A Large Strain Piezoelectric Microactuator by Folding Assembly

by

Zachary J. Traina

S.B, Massachusetts Institute of Technology (2005)

Submitted to the Department of Mechanical Engineering
in Partial Fulfillment of the Requirements for the Degree of

Master of Science in
Mechanical Engineering

at the

Massachusetts Institute of Technology

June 2007

© 2007 Zachary J. Traina
All rights reserved

The author hereby grants to MIT permission to reproduce and to
distribute publicly paper and electronic copies of this thesis document in whole or in part.

Signature of Author ....
Department of Mechanical Engineering
May 11, 2007

Certified by ....
Sang Gook Kim
Professor of Mechanical Engineering
Thesis Supervisor

Accepted by ....
Lallit Anand
Professor of Mechanical Engineering
Chairman, Committee on Graduate Students
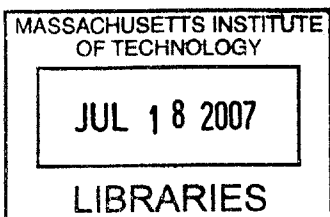
A Large Strain Piezoelectric Microactuator by Folding Assembly

by

Zachary J. Traina

Submitted to the Department of Mechanical Engineering
on May 11, 2007 in Partial Fulfillment of the Requirements
for the Degree of Master of Science in
Mechanical Engineering

ABSTRACT

In-plane amplification of thin film piezoelectric strain has been previously demonstrated using mechanical flexures fabricated at the micro scale. This new work presents a method by which that amplification can be increased, along with a method to reduce parasitic out of plane bending present in prior designs. Fabricated actuator triplets demonstrated peak unblocked displacement of 15 μm, 3% total contraction by length, with an estimated blocking force of ~9.2 μN. Methods of arraying one such cell massively in series and in parallel are also presented, with the long term goal of creating a large strain, efficient, and low power macro scale actuator from individual micro scale components.

Thesis Supervisor: Sang Gook Kim
Title: Professor of Mechanical Engineering

Acknowledgments

Many acknowledgements are due to the people whose contributions in time, knowledge and advice have made this graduate experience a successful and a fruitful one.

First and foremost, many thanks to my advisor Prof. Sang Gook Kim, whose vision for the project and enthusiasm for its potential has been unwavering. Thank you for your patience, encouragement, and support throughout the design process from concept to implementation.

Secondly, many thanks to the many MTL laboratory staff, namely Dave Terry, Dennis Ward, Paul Tierney, Donal Jamieson, Bob Bicchieri, Kurt Broderick, Paudely Zamora, and Scott Poesse, and on the administrative staff Vicky Diadiuk, whose technical expertise and fabrication experience were instrumental in fabricating the devices and many hardware test beds.

Thanks also to my many lab members Robert Xia, Soohyung Kim, Hyungwoo Lee, Stephen Bathurst, Arman Hajati, and Nate Ricker Flynn who have contributed both analytical expertise and critical analysis of design strategy and practice, and have made the MNSL a genuinely constructive place to work and a fertile ground for seedling micro-technology ideas.

Acknowledgement is due finally for the source of the funding for this project, without which none of the following would have been possible: KIMM, The Korean Institute of Machinery and Materials.

Table of Contents

List of Figures

Chapter 1

Introduction

As mechanical systems and devices approach smaller and smaller characteristic dimensions, the need for small form factor, efficient, fast, and powerful actuation technologies is ever increasing. Typical applications for micro scale actuators span several fields where fast, small form factor actuation is required. Direct actuation is needed in micro-optics and electronics, where actuators activate relays and switches and control mirror arrays for displays and telecommunications [1-3]. Microactuators drive pumps and valves in micro Total Analysis Systems (μ-TAS) [4] and other microfluidic or small volume chemistry systems such as Lab on Chip (LOC) systems [5] and ink jet print heads [6], among others. The small form factors of microactuators lend them additional stiffness to weight ratios and high resonant frequencies [7], making them ideally suited for fast response precision tasks such as in AFM heads and high density data storage devices [8].

At the micro scale, linear actuators are of particular interest given their flexibility and relative fabrication simplicity in comparison to rotary systems. Linear actuators can be monolithically constructed without complicated mechanisms such as micro bearings and gears, decreasing their complexity and eliminating wear associated with moving parts. In this area a great deal of research has been dedicated to the development of "smart" materials and alloys which generate motion from an electrical stimulus or chemical reaction.

Conducting (or conjugated) polymers such as activated polyacylonitrile (PAN) fibers and polypyrrolle (PPy) composites demonstrate length variance when they undergo reduction-oxidation reactions in an aqueous environment, expanding or contracting as they incorporate or expel elements into the polymer backbone. The redox reaction can be stimulated by electrochemical doping and undoping [9], and can result in large (but low frequency) strains from ~12 to 400% [10]. Shape memory alloys such as nickel titanium demonstrate strain by phase change in the material from martensite to austentite as the material is heated. Shape memory alloys have tremendous energy density, can exhibit

9

large strain up to 8% and significant blocking force up to 500 MPa at relatively high frequencies, but are inherently inefficient and power intensive due their dependency on temperature change for contraction or elongation [11]. Dielectric elastomers are a class of electroactive polymers that take advantage of the Maxwell stress generated in an insulator subjected to an electric field. These materials are able to generate up to 200% strain and 7 MPa stress, with appreciable efficiency greater than 80% [12-14].

Of the aforementioned technologies, many are able to generate high stress and strain, with excellent energy density and cycle lives. However, not one of these materials is able to provide this work output at high frequency, with high efficiency and at low power. In the case of conducting polymers, the speed of the chemical reaction limits the cycle time to seconds or more. Smart memory alloys, despite their high strength and large strain, are inefficient and demand large amounts of power in resistive heating. Dielectric elastomers allow for large stress, strain, and high efficiency, but also require tremendously high voltages to actuate. In the case of electrostatic actuators, very large form factors and/or voltages must be implemented in order to generate significant force. Further improvement is needed to meet the demands of fields like mobile robotics, which require large stress and strain and fast actuation, as well as high efficiency and low power operation.

Piezoelectric materials such as Lead Zirconium Titanate, Barium Titanate, and a host of other electroactive ceramics provide high frequency, large force, and highly efficient electromechanical transduction. In a thin film formulation, this actuation occurs at very low power, allowing devices to operate with little or no voltage amplification. Piezoelectric thin films are compatible with standard MEMS manufacturing technologies, and can be fabricated, patterned, and integrated into small scale devices. Two major obstacles must be overcome in order for a PZT-based microactuator to compete with other technologies: firstly, the strain of piezoelectric materials is typically very limited, and therefore must be greatly amplified. Secondly, because these actuators are fabricated via planar 2D lithography, some method of assembling devices volumetrically, not just in plane, must be developed in order to enable these devices to perform actuation in macro scales.

Strain Amplification. In-plane displacement amplification of PZT thin films has been demonstrated at the micro scale [15]. These results are encouraging in terms of piezoelectrics' potential as a high speed, efficient, large strain and high force actuation solution in solid state. In order to compete with other actuation technologies however, the strain must be further increased. The un-amplified strain of a thin film piezoelectric is no more than ~0.1 − 0.2%, which means that the strain amplification (not just the displacement amplification) must be on the order of at least 10:1 or more in order to generate useful strain in the range of a few percent.

"En Masse" Assembly. In addition to the development and optimization of a single PZT based actuator, this work attempts to develop a fabrication process that jointly enables assembly "en masse" and facilitates the collection of several batch fabricated devices into a single aggregate system. If a significant number of actuators is assembled, the collection constitutes a multi-scale assembly, where the characteristic dimension of the complete device is orders of magnitude larger than its smallest component. A multi-scale assembly has the advantage of leveraging the favorable properties of smart materials that may only exist at the small scale: in the case of shape memory alloy (SMA), increased speed of heat transfer for example, or in the case of thin film piezoelectrics, low operating voltage, while still functioning at a large scale. If the components are similar to one another and modularly assembled, the collection becomes easily scalable, down to a single unit. The resolution of the collection is limited only by the resolution of the smallest individually controllable section. Practical assembly is the only remaining technological impediment to the realization of a multi-scale actuator.

In the case of micro scale components, assembly is technologically difficult and typically very expensive due to the size of components and the accuracy with which they must be positioned. This added expense is ironic given that individual MEMS devices are cost-effective and benefit from economy of scale precisely because they can be constructed monolithically (with no assembly requirements at all). Unfortunately, integration of devices with widely varying materials and process conditions invariably necessitates some type of mechanical assembly. To address this issue several automated assembly techniques have been developed, which can be classified broadly as either "serial" processes, where devices require individual attention to be assembled, or

"parallel" or "batch" processes, where a large number of devices can be constructed in a single action. Hollis and Rizzi [16] identify several assembly technologies at the state of the art:

Robotic Serial Assembly. If the amount of manual manipulation becomes too intensive for humans, robots with an array of microgrippers and micro positioners [17,18] can be used to fixture and fasten MEMS assemblies. Though technologies have been suggested to fixture components statistically using passive trapping [19], assembly of this nature is still a serial process, since components must be located, gripped, manipulated, and fastened one at a time. The problems of robotic micro assembly are similar to the problems of macro scale assembly; specifically finding, orienting, and positioning parts consistently and without damaging them. Typical serial assembly operations such as pick-and-place automated robotics are time consuming and delicate since assembly effort scales linearly with the number of integrated components. Serial assembly allows very complex structures to be built however, since each device is manipulated directly and can have many degrees of freedom about which to move.

Wafer Level Assembly. Batch assembly can be accomplished by bonding entire wafers together to combine features on their surfaces. After bonding two or more wafers, the stack is diced into chips, each containing functional devices. This allows the integration of many heterogeneous processes and materials since features can be generated on separate substrates, so long as they have a common interface to be bonded. Flip Chip technology [20] is another wafer level process, where devices are transferred en masse from one substrate to another.

Self Assembly of Quasi 3D Structures. Surface micromachining can be used to create simple hinges about which large devices can be popped up out of plane [21, 22]. Many devices can be assembled in parallel using batch actuation processes, such as by surface tension effects in a heated solder bead [23, 24], shrinkage effects occurring during the heating of a polymer such as polyimide [25] or by electromagnetic forcing [26]. These

quasi 3D assembly techniques allow for construction of simple devices out of plane of the wafer, such as micro mirrors and lenses.

Demonstrated batch (parallel) assembly operations thus far have shown en masse assembly of several micro devices across the surface of a wafer, and of course there are numerous demonstrations of many devices being assembly into one micro-system, but to the author's knowledge there is no current demonstration showing batch processed, large scale manipulation, integration and assembly of several modular devices into a single unit. For several micro actuators to operate on the same end effecter, these are all necessary, but absent, functionalities. This assembly process would be an enabling technology for a PZT-based macro scale actuator comprised of micro scale components.

Chapter 2

Background: Piezoelectricity

The Piezoelectric Effect. Piezoelectricity, first discovered by Jacques and Pierre Curie in the 1880's, is a measure of the coupling between the electrical and mechanical behaviors of a given material. As a strain is applied across a piezoelectric material, a voltage develops on the material's surface. Conversely, a voltage applied to the material generates a slight strain. Piezoelectric materials, due to their comparatively high operating frequency, generous maximum force and high operating efficiency [27] have found widespread use in electronic frequency and sound generation (sonar), in actuation and transduction (pressure sensors, AFMs, STMs, ink jet printers, speakers), and as high voltage sources (medical ultrasound, electric lighters).

Polarization and Hysteresis. The electromechanical coupling in piezoelectric materials arises from charge asymmetry in the basic repeating cell of the crystal lattice. This natural polarization is exaggerated as the cell is flexed, twisted, or compressed, developing a potential difference across the crystal structure. The piezoelectric effect is particularly strong in ABO_3 perovskite type materials, including Barium Titanate ($BaTiO_3$), Lithium Niobate ($LiNbO_3$) and Lead Zirconuim Titante, or PZT ($Pb(Zr,Ti)O_3$). This bulk of this work is based on the properties of the latter, and thus the remainder of this discussion disregards other classes of piezoelectric materials although they are plentiful. In a perovskite crystal structure, the charge asymmetry results from the displacement of a small tetravalent center ion, such as titanium or zirconium, from the surrounding lattice formed by a divalent metal ion such as lead. The cubic (unstrained) and tetragonal (strained) forms of the perovskite crystal phase are shown in Figure 1. Since the centers of charge are functions of position only, the potential generated is directly proportional to the applied strain and vice versa, and is directionally dependent such that an opposite stress applied to the bulk results in an equal but opposite electric field.
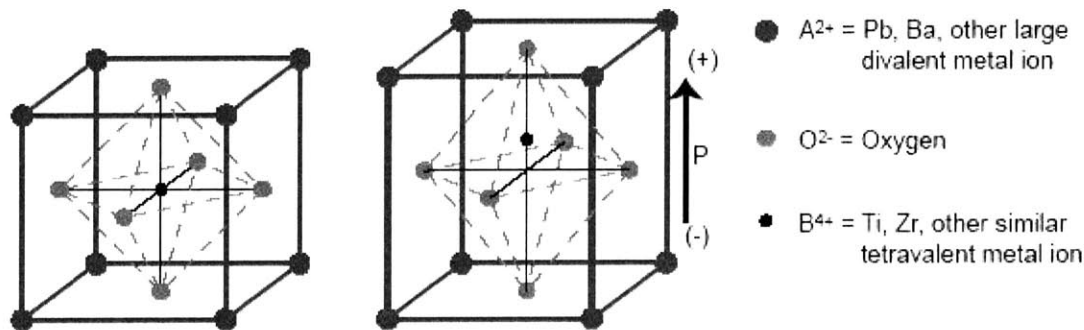
Figure 1: Tetragonal and cubic forms of perovskite crystal structure.[1]

Though each crystal cell (dipole) has a natural polarization, the adjacent cell or group of cells may not be similarly aligned immediately after growth. Random alignment of adjoining dipoles, or domains, throughout the bulk results in zero net polarization of the bulk ceramic. In order to align grains to one another, a strong electric field is applied that "poles" each cell, slightly elongating it in the direction of the field. After the field is removed, the cells relax but some permanent realignment remains, resulting in net polarization of the material as a whole. For small voltages, the piezo will expand in a roughly linear manner. As the voltages are increased, the piezo will re-pole itself in the direction of the field, or, if the voltage is too great, will short as dielectric breakdown occurs in the piezoelectric layer. In this case, the spark that jumps from one electrode to the other will irreparably damage the piezo. For PZT, the electric field must be on the order of about 100V/cm in order to completely pole the structure. Dielectric breakdown occurs at about 40V/μm.

Because of the time dependency of the piezo due to polarization, the total deflection will lag behind the applied voltage as domains are realigned with the applied field. This leads to a butterfly or hysteresis curve as shown in Figure 2.

[1] *Image:* Du Toit, N, and Kim, Sang Gook (2005): "Modeling and Design of a MEMS Piezoelectric Vibration Energy Harvester", M.S. Thesis, Massachusetts Institute of Technology.
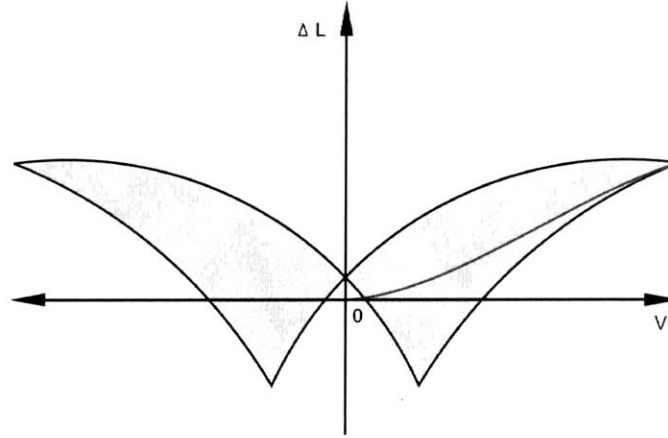
Figure 2: Piezoelectric butterfly curve.[2]

Sol Gel PZT. Thin films of PZT may be fabricated by several methods, including sputtering [28], laser ablation [29, 30], screen sprinting [31], chemical vapor deposition [32], and chemical solution deposition (CSD) processes [33, 34], of which sol gel deposition may be considered a subset. Sol gel deposition is an attractive option for thin film fabrication because it does not require complicated equipment and is therefore relatively inexpensive for small scale production [35], and can generate relatively thick films (up to 0.5 µm) at temperatures less than 700C. Sol gel deposited films also tend to be more uniform in composition than sputter deposited films since reactants are allowed to intermix at the molecular level while in solution.

The PZT sol is a colloidal suspension of Lead Acetate (Pb(CH$_3$CO$_2$)2 3H$_2$O), Zirconium-tetra-n-butoxide (Zr(n-OC$_4$H$_9$)$_4$) and Titanium-terta-iso-propoxide (Ti(i-OC$_3$H$_7$)$_4$) in a 2-Methoxyethanol solvent. The solid solution is spun onto a flat surface at 2000-3000 RPM and quickly dried to remove the solvent, causing the suspended particles to precipitate to a condensed, gel-like film. During pyrolysis at slightly higher temperature, the particles sinter into an amorphous thin film. Several thin films can be deposited on top of one another to develop a total film thickness up to several hundred nanometers, though the increased thermal cycling tends to degrade the quality of the final film. The perovskite phase of PZT forms during a high temperature (approximately 650 C) anneal following deposition.

---

[2] Image Courtesy Physik Instrumente. http://www.physikinstrumente.com/en/

16

Crystal Nucleation and Growth. It has been well documented that the transformation of the amorphous phase to the perovskite phase of PZT is largely dependent on the temperature of pyrolosis and the duration and temperature of the following anneal [36]. Particular care must be taken during temperature processing of the film to prevent the formation of the stable pyrochlore phase, which exhibits no piezoelectric properties. To catalyze perovskite growth during the anneal (ie, to compensate for lead deficiency which forms during the volatile diffusion of Pb ions during processing), a lead-titanate (PT) seed layer may be deposited on the substrate prior to the initial PZT sol gel deposition. The substrate itself is evaporated Pt/Ti on SiO_2 (thermally oxidized Silicon), which has proven to be a beneficial substrate for PZT film growth due to the particular crystal structure at the surface which provides numerous nucleation sites for perovskite crystal instigation [37, 38]. The oxide serves as a diffusion barrier, preventing the highly volatile Pb ions from diffusing into the underlying Silicon during the high temperature anneal. Annealing the PZT film on bare oxide may cause severe delamination or cracking as the PZT reacts chemically with the silicon [39,40]. To prevent this reaction the film is patterned prior to annealing such there is very little direct contact between the substrate and the piezoelectric layer.

Figure 3 shows an SEM image of PZT grains developed after deposition, drying, pyrolyzing, and annealing to a thickness of 0.4 μm. Grain sizes are consistent with the literature for a film of this thickness [41].
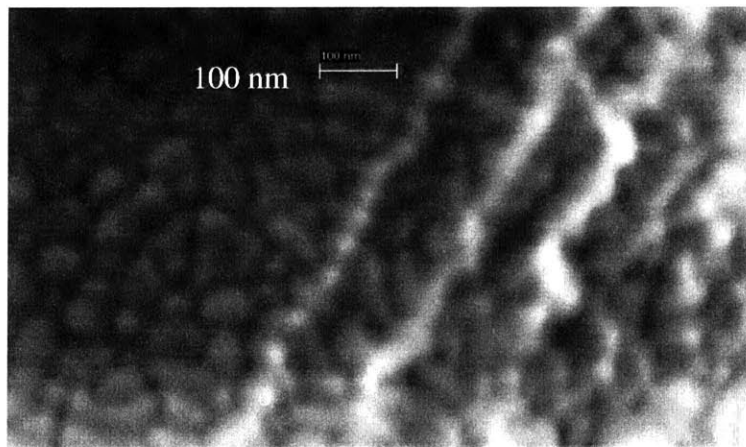
Figure 3: SEM of PZT grains on Pt substrate after annealing. Separate layers of PZT are clearly visible to the right, where etchant has patterned the crystal preferentially along specific crystallographic axes.

Thin Film PZT Performance. The mathematical nature of electro-mechanical coupling in the piezoelectric is described by the material's constitutive equation, which takes the form:

$$S = s_E \cdot T + d^t \cdot E \qquad (2.1.1)$$

$$D = d \cdot T + \varepsilon_T \cdot E \qquad (2.1.2)$$

where the state variables T, D, S, and E represent the material stress, charge-density displacement, strain, and electric field, and ε is the material permittivity. The matrices d and s_E contain the material's piezoelectric and compliance constants, which for PZT-4 are:

$$s_E = \begin{bmatrix} 12.3 & -4.05 & -5.31 & & & \\ -4.05 & 12.3 & -5.31 & & & \\ -5.31 & -5.31 & 15.5 & & & \\ & & & 39 & & \\ & & & & 39 & \\ & & & & & 32.7 \end{bmatrix} * 10^{-12} \frac{m^2}{N} \qquad (2.1.3)$$

$$d = \begin{bmatrix} & & & & 496 & 0 \\ & & & 496 & & \\ -123 & -123 & 289 & & & \end{bmatrix} * 10^{-12} \frac{C}{N} \qquad (2.1.4)$$

18

Note that the film deposited by sol gel is not precisely the crystalline formation of PZT 4A for which constants are given above. Because the experimental determination of these coefficients is non-trivial, constants for PZT4A are used only as an initial approximation for early design revisions.
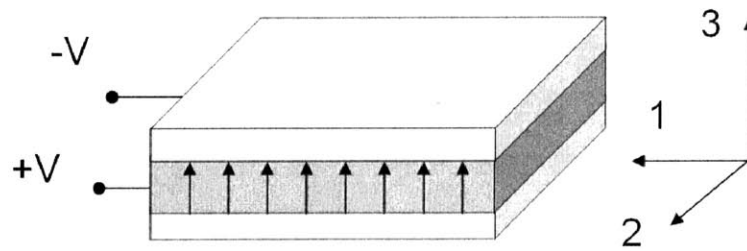
Figure 4: Direction conventions for PZT actuation.

The directional convention shown in Figure 4 is used, where the directions 1 and 2 are in the plane of the thin film piezo and direction 3 is normal to the film surface. Thus d_{33} relates the material's deflection out of plane when subjected to a parallel voltage field, and d_{31} refers to the material's in-plane deflection under the action of the same field. Orthogonal deflection in d_{31} mode is not a direct effect of piezoelectricity, but rather an effect of the material's tendency to conserve volume as deflects in the out of plane direction.
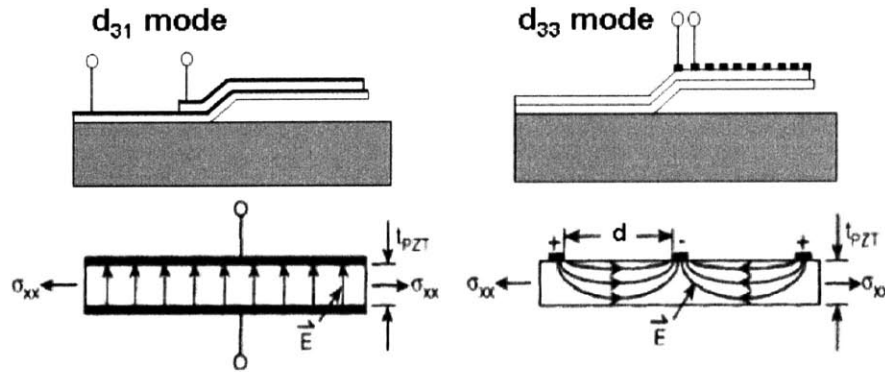
Figure 5: D_{33} and D_{31} modes of PZT thin film. [3]

Devices that utilize these two modes are shown in Figure 5. In d_{33} mode, polarization and the deflection of interest are parallel to one another. In one implementation, interdigitated electrodes span one surface of the PZT thin film, and polarization wraps from one electrode to the next in alternating directions. In d_{31} mode, the electrodes span both the top and bottom surface of the piezo. As in d_{33} mode, polarization and elongation occur in the same direction, in this case out of plane. However, the ends of the piezo in d33 mode are typically constrained to make use of the orthogonal expansion or contraction. Observing the d_{33} and d_{31} constants, it is clear that the orthogonal induced strain in d_{31} mode is about one third that of its d_{33} counterpart, but because the separation between electrodes in this mode is just the thickness of the PZT layer, the device can be poled at very small voltage. For PZT layers 0.5µm thick, the device can be poled with less than 10V.

The maximum stress and strain of the thin film can be developed from the constitutive equation. In the d_{31} mode, the out of plane direction is unconstrained, and stresses in this direction are therefore set to zero. The in plane deflection then, is

$$x_1 = \left(s_{11}^E + s_{12}^E\right)\sigma_1 + d_{31}E_3 \qquad (2.1.5)$$

---

[3] Image: J.J. Bernstein, J. Bottari, K. Houston, G. Kirkos, R Miller, B. Xu, Y. Ye, and L.E. Cross, "In Plane Polarization for High Sensitivity Ferroelectric MEMS Ultrasound Transducers," Applications of Ferroelectrics, 2000. ISAF 2000. Proceedings of the 2000 12th IEEE Symposium.

assuming the poling direction is out of plane and shear forces are negligible. This may be set to zero to determine the maximum stress (and blocking force if the cross section is known), ie

$$\sigma_{max} = \frac{d_{31}E_3}{\left(s_{11}^E + s_{12}^E\right)}$$

(2.1.6)

or conversely, if the stress is zero, the maximum in plane strain

$$x_{max} = d_{31}E_3$$

(2.1.7)

In most cases, the total strain that can be developed by a piezoelectric material is very small, on the order of 0.1-0.2%, due to the small d_{31} constant and the upper bound on the electric field imposed by the risk of dielectric breakdown in the film.

Chapter 3

Device Design

An axiomatic development framework is employed during the design in order to minimize complexity and maximize the chances of success. Axiomatic design is the practice of reducing project goals to a complete, but independent, set of functional requirements (FRs) that describe the critical objectives of the design. Each of these functional requirements is then mapped to a physical solution, or design parameter (DP) that addresses the requirement.

For this device, the major design objectives are to efficiently amplify the strain of PZT and to be able to array that amplifier massively in series and in parallel assuming it is constructed at the micro scale. The following functional requirements are identified:

FR1. Demonstrate large contractive strain in the direction of force actuation.

FR2. Exhibit planar actuation without parasitic bending.

FR3. Device must be arrayable en masse.

To address each functional requirement, the following design parameters are chosen:

DP1: Amplifying beam superstructure increases strain.

DP2: Mid-plane PZT eliminates the eccentric load responsible for plane bending.

DP3: Gold ribbon hinges provide amass assembly solution.

FR1. Large Strain. The requirement for high strain output from each actuator cell precedes all other functional requirements. Specifically, large contractive strain in the direction of force actuation is desired, so it is assumed that large total displacements may be developed through the use of several actuators in series. Since strain is by definition the degree of elongation per unit length, the total strain may be increased either by enlarging the total stroke or by decreasing the axial dimension. This design attempts both

22

by optimizing the hinge geometry to provide maximum stroke in a minimal axial footprint.

Though many piezoelectric amplification schemes exist [42], a moonie actuator is chosen for several reasons, mostly for its suitability in amplifying very small input displacement, relatively straightforward fabrication process, and small axial footprint. Additionally, success had been shown by the author's predecessor using a moonie type design and optimizing the existing geometry seemed to be a logical development direction towards the achievement of a large strain, highly arrayable actuator. This work, done by Nick Conway and Sang Gook Kim [15], is shown in Figure 6, which has an extensional strain as the piezoelectric member contracts.
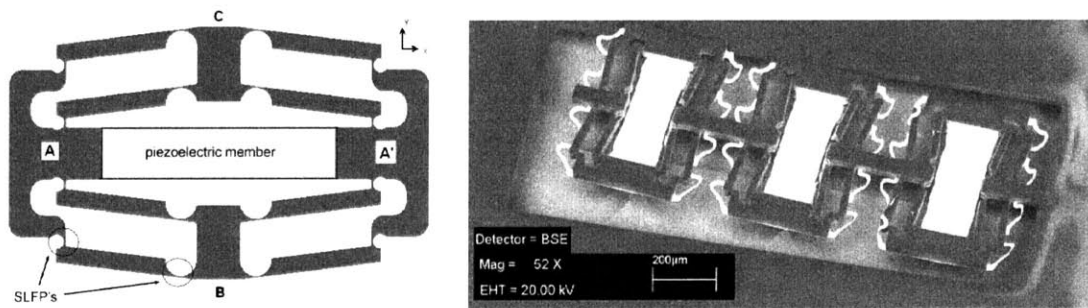
Figure 6: A saggital amplifier for the amplification of in plane piezoelectric strain, by Nick Conway and Sang Kim, [15] *Left*: Conceptual schematic. *Right*: Three devices fabricated in series.

The core of the design is a saggital amplification structure, constructed from a high aspect ratio SU8 polymer, which amplifies very slight input displacement via the rotation of hinged beams. The actuating member is a .48 μm thick PZT beam that supplies an input displacement of approximately .38 um. As the input nodes A and A' are drawn slightly together, the output nodes B and C contract with greatly amplified displacement. Opposing four bar linkages ensure that the end effecter moves linearly as the device expands. The ratio of input displacement to output displacement (or amplification) depends heavily on the initial angle α formed between the line joining the cantilever hinges and the horizontal.
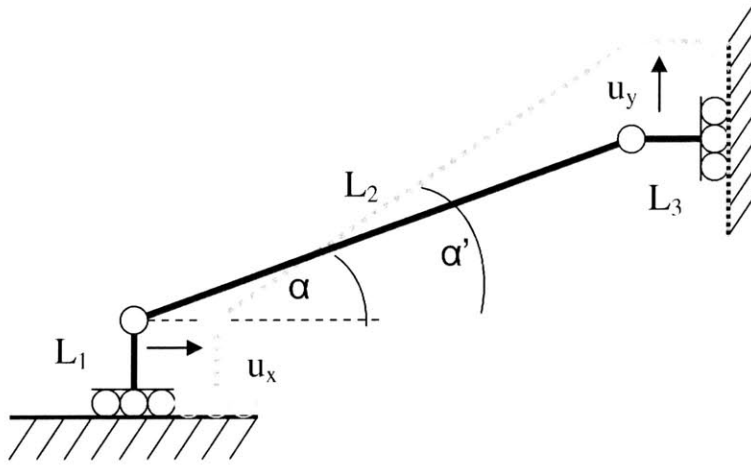
Figure 7: Amplification principle.

Figure 7 shows a reduced model of the device, shown as a simple three bar system with pure rotational joints. Please note that the following analysis is adapted from Lebontiu [43], who gives an energy analysis for an equivalent 4 armed device with 8 flexural hinges. The displacement amplification in terms of this coordinate system gives:

$$u_1 + l_2 \cos\alpha' = l_2 \cos\alpha \tag{3.0.1}$$

$$l_2 \sin\alpha' = l_2 \sin\alpha + u_y \tag{3.0.2}$$

$$a = \frac{u_y}{u_x} = \frac{\sin\alpha' - \sin\alpha}{\cos\alpha - \cos\alpha'} \tag{3.0.3}$$

or, in terms of the initial angle only,

$$a = \frac{u_y}{u_x} = \sqrt{\frac{l_2^2}{u_x^2 \sin^2\alpha} + \frac{2l_2}{u_x \cos\alpha} - 1} - \frac{l}{u_x \sin\alpha} \tag{3.0.4}$$

The system may also be analyzed in terms of stiffness by redrawing the schematic with linear springs approximating each of the input and output stiffnesses K_{in} and K_{out}, as shown in Figure 8. These stiffnesses are the two equivalent elastic resistances encountered by input forces at the two endpoints of the amplifying beam. The schematic is one for two wedges sliding over one another without friction. Here the assumption is made that the amplification ratio does not vary greatly with displacement, which is reasonable for small angles of deflection.
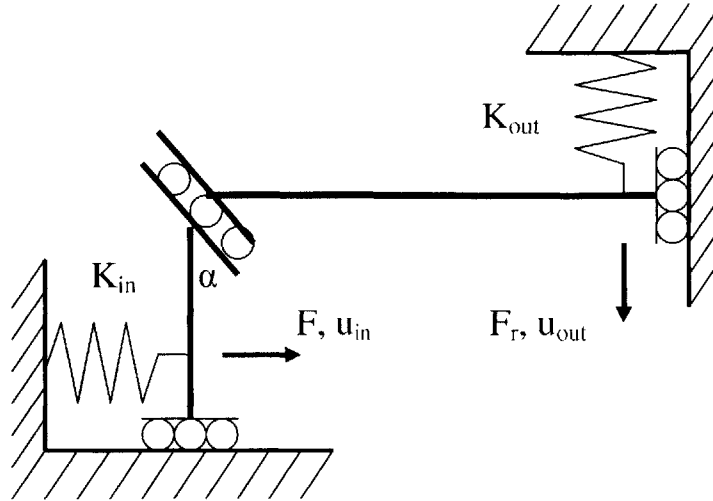
Figure 8: Amplification principle considering limited input and output stiffness.

With both an input and an output force applied to the system, energy conservation gives the following relationship:

$$\frac{Fu_{in}}{2} = \frac{F_r u_{out}}{2} + \frac{K_{in} u_{in}^2}{2} + \frac{K_{out} u_{out}^2}{2}$$ (3.0.5)

which, when combined with the geometrical relationship

$$\tan \alpha = \frac{u_{in}}{u_{out}} = \frac{1}{a}$$ (3.0.6)

gives the formulation relating amplification, a, input and output forces, and input and output stiffnesses together at a given instant

$$F - aF_r = \left(K_{in} + a^2 K_{out}\right)u_{in}$$ (3.0.7)

Note that when the vertical load on the system is zero, and the input force on the system is constant, this reduces to

$$u_{in} \sim \frac{1}{K_{in} + a^2 K_{out}}$$ (3.0.8)

and when both forces are zero, Lebontiu finally concludes that the initial amplification ratio is

$$a^2 = -\frac{K_{in}}{K_{out}}$$
(3.1.9)

so the net amplification ratio is related to the ratio of the input to output stiffness. In order to achieve maximum strain, the input displacement must be maximized in addition to the amplification. The original functional requirement can therefore be subdivided into secondary requirements:

FR_{11}: Amplification ratio of the beam structure is maximized.

FR_{12}: Input displacement to the beam structure is maximized.

These two functional requirements depend in opposite ways on K_{in}, which suggests that the amplifying structure must find an intermediate balance. The following analysis shows however that the input stiffness of the amplifying structure is negligible in comparison to the electrode stiffness, and therefore has minimal effect on the net input displacement. The design parameters, then, become

DP_{11}: The ratio $a^2 = -\frac{K_{in}}{K_{out}}$ is maximized.

DP_{12}: The stiffness of the laminated electrodes is minimized.

3.1 FR_{11} with DP_{11}: Amplification Ratio

The resultant design is shown in Figure 9. Geometry changes have been made to the device length and thickness, as well as the hinges to increase the total stroke. The device operates in contraction, so the four beam linkage is unnecessary to maintain linearity of the end effecter and is removed.
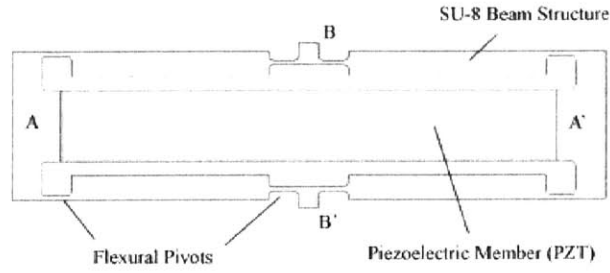
Figure 9: Front view of a single actuator.

Flexure pivots are used in place of traditional pin joints in order to minimize fabrication complexity. Monolithically fabricated hinges also eliminate problems associated with backlash that would be catastrophic in this case given the very limited initial displacement. The geometry of the flexure pivots and their placement relative to one another in the flexure control both the input and output stiffness, and therefore a bulk of the performance of the actuator, so they are given thorough analysis here.

Reducing the number of arms in the device requires increasing the cross sectional area of the hinge, since the blocked PZT force approaches the yield stress of the amplifying beam structure (assuming it is still constructed from a polymer such as SU8 resist). A straight cantilever type hinge is employed to prevent undue amplification of the joint stiffness, and thus the stored energy, in the hinge as it rotates. Of the implementable hinge types (right circular, cantilever filleted, and elliptical, among others), the cantilever type has the most flexibility and is therefore best suited to large displacement applications according to Xu and King [44]. This change still constitutes a net increase the joint stiffness using relations developed by Smith [45]:

$$K_{notch} = \frac{2Ep}{9\pi}\sqrt{\frac{t^5}{R}} \tag{3.1.1}$$

$$K_{cantilever} = 2\gamma K_\theta \frac{EI}{L} \tag{3.1.2}$$

using $\gamma = .852$, and $K_\theta = 2.67$ determined experimentally, but the energy stored in the hinges is small compared to the total work done by the end effecter, and the slight loss is far outweighed by the benefit of greatly reducing the total device height. In flexure hinge design the increased stiffness leads typically to increased maximum tensile stress in the

hinge at its greatest deflection, which compromises its cycle life. However, because this device is under a large axial compressive load, the bending stress is not the dominant stress in the system and this consequence is ignored.

The high flexibility of the cantilever hinge comes at the price of accuracy, but because this device is designed as one member of a large matrix, it is assumed that small errors will disappear in the aggregate motion of the entire actuator collection. The stiffness ratio of the cantilever hinge itself is maximized when the longitudinal and lateral forces on the cantilever are aligned exactly parallel and perpendicular to the long axis. For any rotation away from these axes, the ratio decreases, so the hinges are implemented in parallel with the working axis of the piezo.

Without co-locating any features (ie, overhanging the amplifying structure on top of the PZT beam), this device has a near optimal footprint in terms of energy density, since the active PZT area occupies a majority of the space. With basic geometry determined, the actuator may now be analyzed as a composite beam structure.
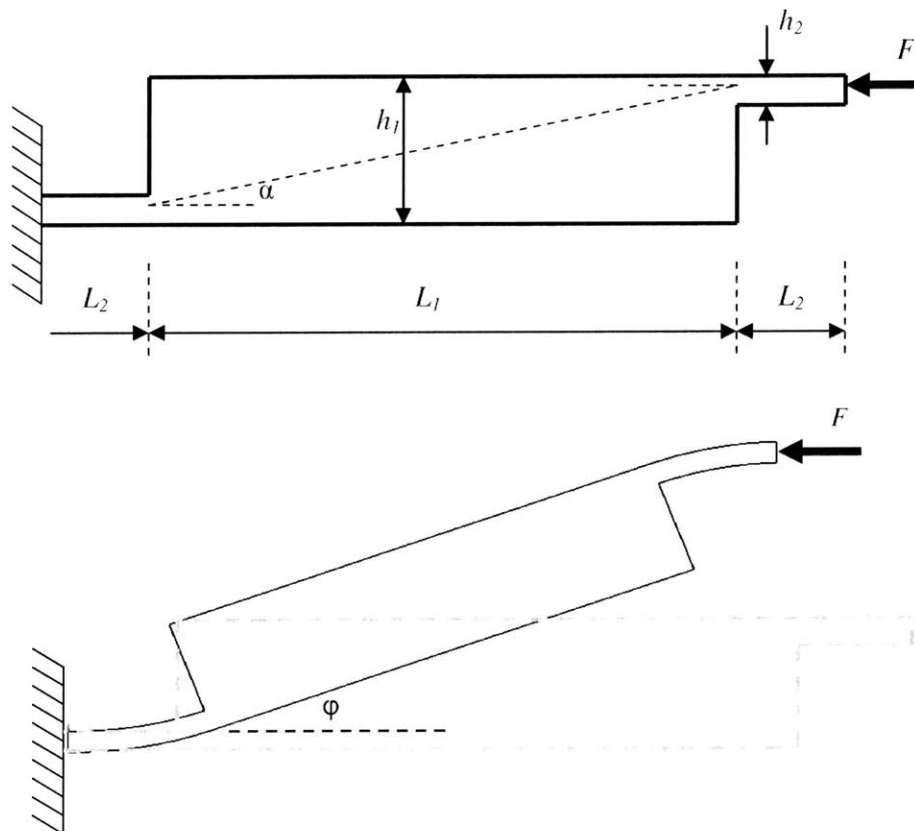
Figure 10a, b: One arm of the device before and after deflection.

A quarter model of the device, just one of the four rotating beams, is shown in Figures 10a and 10b. The rotating beam has height h_1 and length L_1. The cantilever hinges have height h_2 and length L_2, and are spaced vertically by the initial angle α. As either the piezo force F or a vertical force F_L is applied, the structure deforms to the shape in Figure 9b, where the beam has rotated an additional angle ϕ.

From equilibrium of the entire system, the moment on the two hinges can be determined:

$$M = -M_R = \frac{Fh_1}{2} \tag{3.1.3}$$

$$h_1 = \frac{L_1}{\cos\alpha}\sin(\alpha + \phi) + 2L_2\sin\frac{\phi}{2} \approx (L_2 + L_1)\phi + L_1\alpha \tag{3.1.4}$$

and the angle of deflection of the center member, ϕ, is approximately:

$$\phi_{max} = \frac{ML_2}{EI} = \frac{12L_2}{Ebh_2^3}\left(\frac{F}{2}\left(\frac{L_1}{\cos\alpha}\sin(\alpha + \phi) + 2L_2\sin\frac{\phi}{2}\right)\right) \tag{3.1.5}$$

Using small angle approximations for *sin* and *cos* and collecting terms:

$$\phi_{max} = \frac{6L_2 F}{Ebh_2^3}\left(L_1\alpha + (L_1 + L_2)\phi\right) \tag{3.1.6}$$

$$\phi = \frac{Ca}{1 - Cb}, \quad C = \frac{6L_2 F}{Ebh_2^3}, \quad a = L_1\alpha, \quad b = (L_1 + L_2) \tag{3.1.7}$$

The horizontal deflection of a single flexure (or the center section) with combined moment M_R and compression F is:

$$\delta_{2x} = \frac{FL_2}{A_c E} = \frac{FL_2}{bh_2 E} \tag{3.1.8}$$

$$\delta_{1x} = \frac{FL_1}{bhE} \tag{3.1.9}$$

The endpoint of the flexure arm also moves horizontally as the beam bends, shortening the horizontal projection of the member according to

$$\Delta l = -\frac{1}{2}\int_0^l \left(\frac{dy}{dx}\right)^2 dx \tag{3.1.10}$$

but for the small angle of deflection involved this number is comparatively small and is ignored. The total horizontal deflection of the endpoint is then:

$$\Delta x = \delta_{x1} + \delta_{x2} + \delta_{x3} + \frac{L_1}{\cos \alpha}\left(\cos(\alpha + \phi) - \cos \alpha\right) \tag{3.1.11}$$

The vertical deflection of the endpoint is simply the height h_1 minus the initial separation between hinges, expressed as

$$\Delta y = \frac{L_1}{\cos \alpha}\left(\sin(\alpha + \phi) - \sin \alpha\right) + 2L_2 \sin \frac{\phi}{2} \tag{3.1.12}$$

since the contributions due to the bending hinges are equal and opposite, and therefore cancel out. The strain amplification for the device with compressible elements, finally, is:

$$A = \frac{\Delta y}{\Delta x} = \frac{\dfrac{L_1}{\cos \alpha}\left(\sin(\alpha + \phi) - \sin \alpha\right) + 2L_2 \sin \dfrac{\phi}{2}}{\delta_{x1} + \delta_{x2} + \delta_{x3} + \dfrac{L_1}{\cos \alpha}\left(\cos(\alpha + \phi) - \cos \alpha\right)} \tag{3.1.13}$$

which agrees with Conway's result with the exception of the additional compression elements in the calculation of Δx and the addition of significant hinge length, L_2. These slight compression elements preclude the theoretical possibility of infinite amplification for very small α values, since the horizontal deflection levels out at a constant value while the output deflection proceeds to zero. This creates a peak in the maximum possible amplification ratio, which is plotted below along with the vertical and horizontal deflections for sample dimensions:

Beam height = 25 μm,

Hinge height h_2= 5 μm,

Device thickness b = 20 μm

Beam length L_1 = 215 μm

Hinge Length L_2 =35

Input Force F = 63 μN, 32.5 μN, and 10.5 μN.
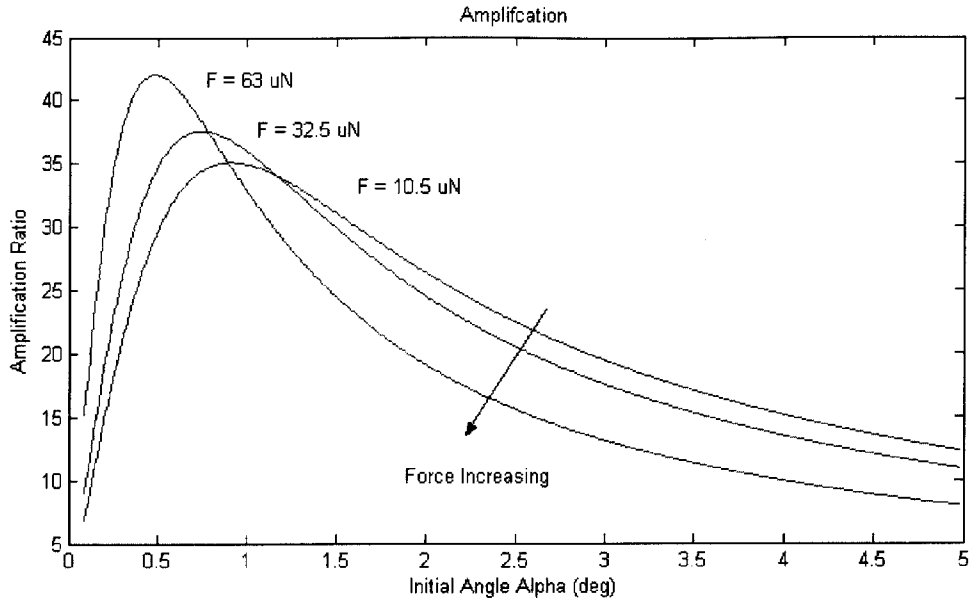
Figure 11: Amplification ratio variance with input force F and initial angle α. As F decreases, so does the angle φ, driving the amplification peak downwards and to the right.

Figure 10 and inspection of Equation 3.1.13 demonstrate that high amplification can be achieved for small forces (or equivalently, small rotation angles ϕ) and initial angles. However, since large rotation angles are needed in order to generate large total output displacements, Figure 10 must be considered jointly with Figure 11, which shows the effect of the initial angle on input stiffness.
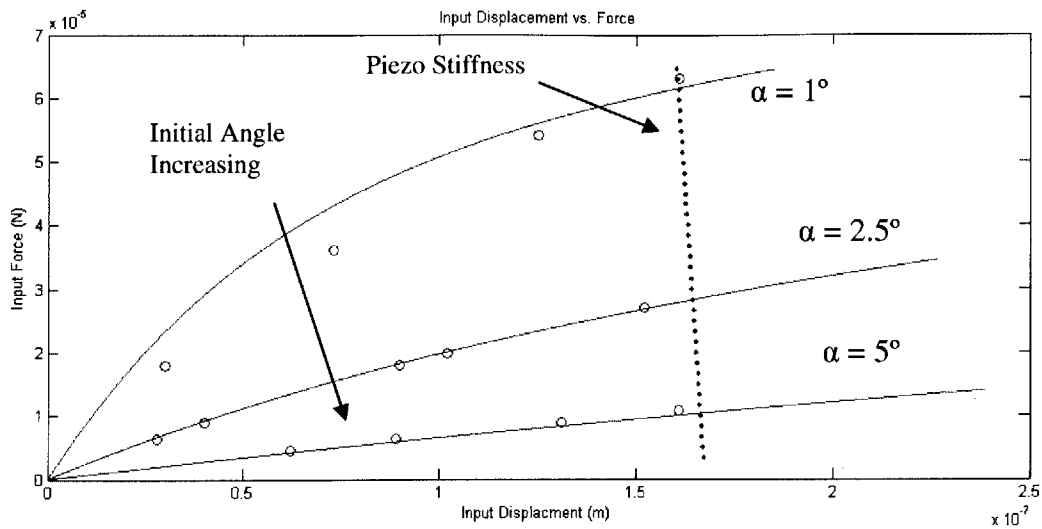
Figure 12: Input stiffness K_{in} characterization for several initial angles. Finite element analysis predictions are shown as open circles, closed form predictions as solid lines.

The flexure strain-softens as it closes, since the moment arm on the rotating beam increases faster than the restoring force applied by the flexure hinges. This gives the roughly quadratic force displacement curve in Figure 12, generated by non linear finite element analysis. By inspection, though the stiffness of the flexure increases by a significant factor as the initial angle decreases, even at very small initial angles the stiffness of the flexure is so small compared to the stiffness of the peizo beam that increasing the initial angle has a negligible effect on the maximum input strain. As in the previous design, then, maximizing the amplification ratio is simply a matter of reducing the initial angle to as small a value as possible.

3.2 FR$_{12}$ with DP$_{12}$: Total Displacement

The maximum input strain is a strong function of the stiffness of the metal electrodes laminated onto the PZT film. As the piezo strains, the force lost parasitically due to the compression of the laminated electrodes is:

$$F = \frac{h_{beam}}{L_{beam}} \left(\sum E_i t_i \right) \delta x \qquad\qquad (3.2.1)$$

with the elastic modulus and thickness values given in Table 1. The stiffness calculated in Eq. 3.2.1 is orders of magnitude greater than the flexure stiffness, so the maximum input strain is driven mainly by the stiffness of the electrodes and other materials laminated onto the PZT film.

Table 1. Material Properties for various thin films.

	Young's Modulus	Layer Thickness	Residual Stress	Source
Gold (Au)	80 GPa	1000 A		IEEE Micro Electro Mechanical Systems Workshop, Feb 1993, Florida, p.25
Titanium (Ti)	110 GPa	400 A		IEEE, Micro Electro Mechanical Systems Workshop, Feb 1990, Napa Valley, California, p.147
Platinum (Pt)	170 GPa	1500 A	185-275 MPa	IEEE Micro Electro Mechanical Systems Workshop, Feb 1990, Napa Valley, California, p.174
Silicon Dioxide	70 GPa	700 A	-275-225 MPa	Thin Solid Films, 283 (1996), p.15 IEEE Micro Electro Mechanical Systems Workshop, Feb 1993, Florida , p.223
PZT	80 GPa	4000A	80-100 MPa	Applied Physics Letters, Sept 2000, Vol. 77 No. 11 pp. 1710-1712. IEEE Micro Electro Mechanical Systems Workshop, Jan-Feb 1991, Nara, Japan. p.118

▨	1000A Gold Au
▨	4000A PZT
▨	750A Platinum Pt
▨	400A Titanium Ti
▥	700A SiO$_2$
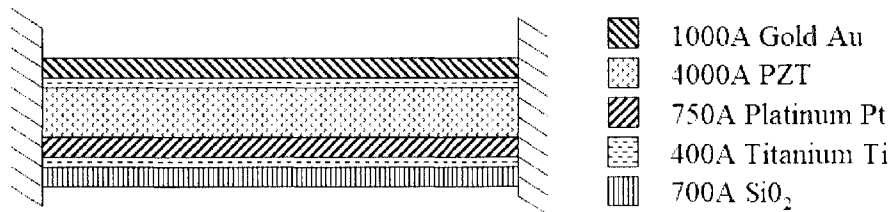
Figure 13: PZT Beam cross sectional structure.

The structure of the PZT beam is shown in Figure 13. Clearly it would be beneficial to reduce the thicknesses and stiffnesses of all the non piezoelectric layers. Because the bottom electrode must nucleate crystal growth in the PZT film, 750A is selected as a practical minimum thickness to guarantee film uniformity. The top electrode has no functional requirements concerning crystal growth, which expands the library of possible materials. Gold is therefore selected due to its low stiffness and excellent conductivity. Titanium and SiO_2 remain on the wafer as artifacts of the manufacturing process. Figure 14 shows the stiffness characterizations of the electrodes vs. the input stiffness K_{in}, along with the force displacement curve of the PZT film. Assuming an unblocked strain of 0.1% and a blocking pressure of ~120 MPa, the maximum strain is reduced nearly in half even with the electrodes significantly thinned.
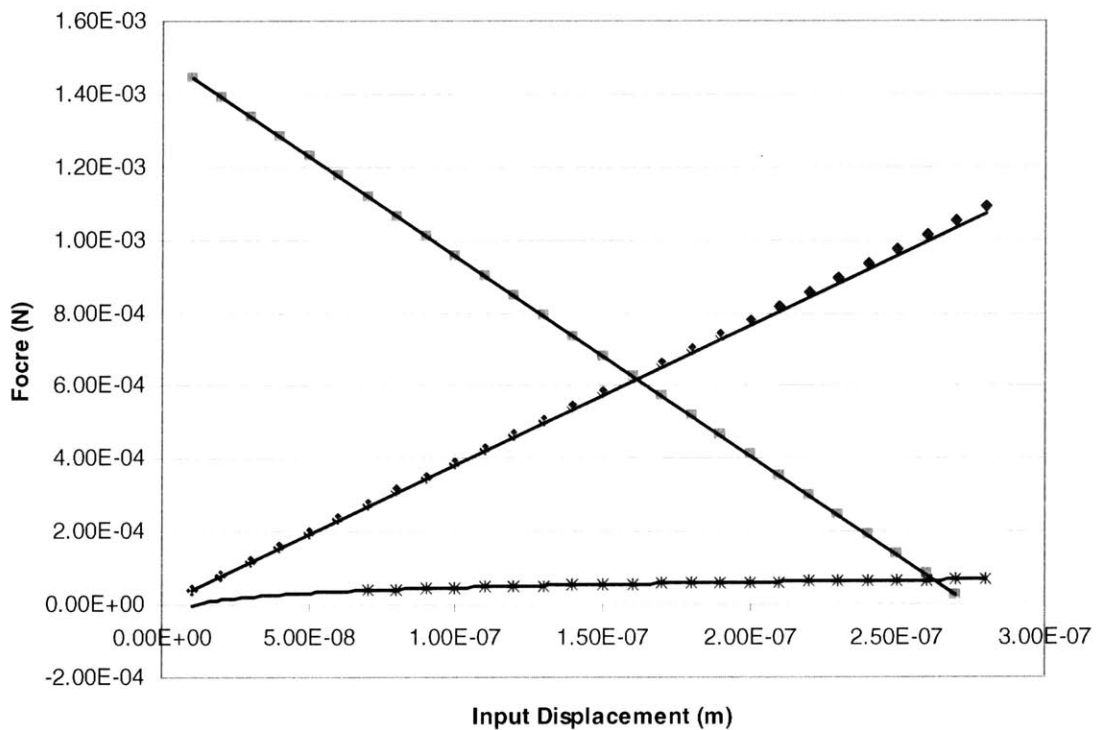
Figure 14: Stiffness characterizations of the flexure (star) and laminated electrode (diamond) vs. the available force from the piezo thin film (square).

The electrodes do not have any effect on the blocking force of the actuator, which is a function of the initial angle and the beam lengths only:

$$F_L = F \frac{L_1 \tan(\alpha)}{(2L_2 + L_1)}$$
(3.2.2)

where F is the input force applied by the piezo and F_L is the applied or output load. For applied loads exceeding F_L, ϕ has a negative value as the flexure opens outwards into a region of instability. Note also that due to the finite stiffness of the beam structure, when the actuator is blocked there is significant axial compression, which reduces the input force F and therefore the maximum sustainable blocked load F_L.

After the device is released from the substrate, residual stresses in the PZT member deform the beam in plane, applying either tensile or compressive load to the PZT strip even with zero applied voltage, which may affect its ferroelectric properties [46]. For now, this complication is ignored in the interest of simplicity and it is assumed that residual stresses in the released device have only a small effect on the mechanical performance of the PZT film. For hinge dimensions 5 µm x 35 µm, and center beam dimensions 25 µm x 215 µm, with a working piezo beam height of 50 µm, the following performance can be expected:

Table 2. Expected Performance values

Performance Metric	Value		
Maximum PZT Pressure	120 Mpa [15]		
Maximum PZT Force	.003 N		
Attenuated Max. Strain	.17 µm		
Device Height	175 µm		
Finite Element Predictions	*1 deg*	*2.5 deg*	*5 deg*
Displacement Amplification	13.27:1	9.83:1	6.36:1
Total Displacement	7.3 µm	5.41 µm	3.50 µm
Effective Axial Strain	4.17%	3.09%	2.00%
Strain Amplification	41.7:1	30.9:1	20.0:1

| Resonant Frequency | - | 5221 Hz | - |

Closed Form Predictions	1 deg	2.5 deg	5 deg
Displacement Amplification	20.36:1	12.38:1	7.56:1
Total Displacement	11.2 μm	6.81 μm	4.16 μm
Effective Axial Strain	6.40%	3.89%	2.38%
Strain Amplification	64.0:1	38.9:1	23.8:1
Blocking Force	7.36 μN	18.4 μN	36.9 μN

3.3 FR₂: Planar Actuation

While the in-plane to out-of-plane stiffness ratio ensures that the beam moves preferentially in the axial direction, some out of plane bending is inevitable as long as PZT beam does not apply force through the structural center of stiffness. Consider the structure in Figure 15, where the amplifying structure is laminated on top of the actuating member. In this case, the out of plane bending is governed by

$$w_{max} = e\left(\sec\left(\sqrt{\frac{F}{EI}} \right)\frac{L}{2} - 1 \right)$$ (3.3.1)

where e is the length of the moment arm between the point of force application and the beam's centroid, L is the beam length, E its elastic modulus and I the moment of inertia. Since the thickness of the piezo is small compared to the rest of the device, the force can be modeled as an eccentric load. Out of plane bending is worst when the actuator is blocked, and F is maximized; in this case the center of the actuator bows ~1.53 μm out of plane. To prevent this undesirable motion the PZT member is relocated to the geometric center of the device, eliminating the eccentric load.
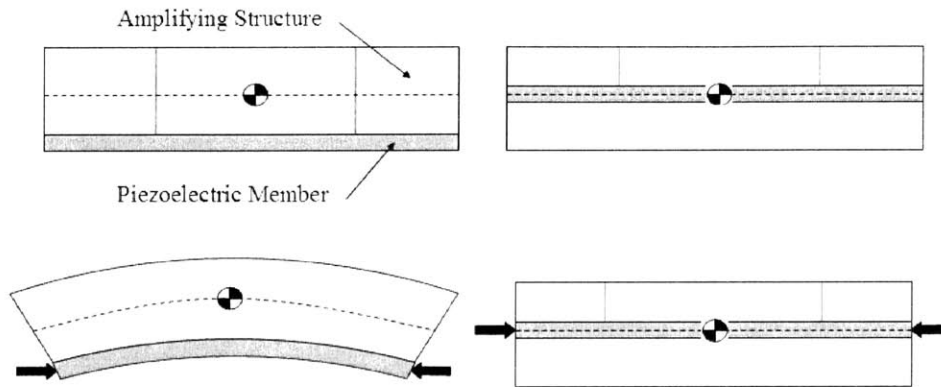
Figure 15: With the piezoelectric member moved from the bottom (left) to the structural center of stiffness of the device (right) there is no eccentric load to cause out of plane bending.

Before the deposition of the SU-8 beam structure the wafer is dry etched in SF_6 to a depth of 10 μm using the PZT beam and wiring layers as masks (See Fabrication details). This effectively depresses the substrate surface, elevating the PZT member to what will become the neutral axis of the flexure.

3.4 FR₃: Arrayability

PZT Beam Design for Reliability. Having a reliably manufactured and durable PZT beam is a crucial requirement for arraying many devices in parallel, since the chance of shorting in a thin film ceramic due to particle inclusions goes roughly as its total area.

Sol gel deposition processes are typically plagued by thickness non-uniformities due to drying effects occurring during the spinning process and particle inclusions from the environment or the solution itself [47]. Without better control of this non-uniformity, the chances of success are vastly increased by limiting the total number of devices connected in parallel at any one time. Non-uniformities also form where the PZT spins over pre-existing topology on the wafer, so the geometry of the bottom electrode should be as simple as possible to prevent unusual particle distribution due to non-newtonian fluid flow over the metal layer edges. This layer is already as thin as possible in order to satisfy FR_{12}.

The incidence of cracking is reduced by placing an upper bound on the film thickness at about 0.48 μm. Thicker films tend to fail as the residual stress in the bulk of the film overwhelms the constraining shear stress at the interface with the substrate [48]. Shorts may also form where the PZT overhangs the Pt surface onto the SiO_2 substrate. This overhang is necessary to prevent the two electrodes from making a direct connection, but can also be problematic since PZT tends to crack when grown on bare Si/SiO_2.

Two approaches are taken to the electrode geometry, shown in Figure 16. In both approaches, the gap between electrodes is minimized to 2.0 - 2.5 μm. In one embodiment, the bottom electrode, PZT, and top electrode are patterned one on top of the other with decreasing outside dimensions. This approach minimizes the amount of PZT which must span bare SiO_2, and has the least chance of failure during processing due to hillocking or cracking. However, after completion the beam is susceptible to shorting by particles that can land on the beam and make a direct connection between the two electrodes. The second design approach is adapted from Y.B. Jeon [49], and prevents the possibility of shorting due to environmental particles by fully encapsulating the PZT member. The first half of the top electrode fully surrounds the bottom electrode, and PZT is deposited over the gap. The second half of the top electrode is deposited last, connecting to the exposed metal on all but one side of the PZT member. The exposed edge will eventually be covered by the SU8 beam structure. This completes a fully encapsulated (and therefore waterproof) PZT beam, which has very low chance of failure when released to the open environment. The chances of failure during manufacturing, however, are greater because of the increased gap length.
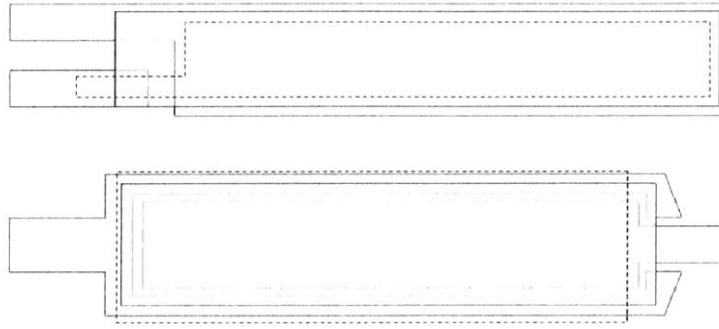
Figure 16: Open (top) and encapsulated (bottom) designs of the PZT member. The solid outlined shapes are the electrodes patterned during the first metal deposition. PZT (green) is then patterned next, and then the 2nd half of the top electrode (dashed).

Long Range Assembly. For long range assembly of many actuators, a multistage approach is taken, where actuators strings are fabricated in arrays or matrices in plane, and then assembled en masse by means of a separate assembly feature. The functional requirements of the assembly feature(s) is to

FR_{31}: Maintain the position of components after their release from the substrate.

FR_{32}: Enable "batch assembly" of components in such a way that manufacturing effort does not scale directly with the number of components.

FR_{33}: Enable assembly "en masse", ie out of plane assembly.

In order not to conflict with the other design requirements already stated, the features must be soft in the direction of actuation in order not to interfere with the maximum strain, and must manipulate devices such that they actuate in the same direction (FR_1). A single design parameter addresses all of the functional requirements:

DP_3: Thin film gold ribbon perpendicular to the direction of actuation constrains devices after release and enables large scale out of plane assembly.

39

Actuators are fabricated in strings in-plane by 2D lithography. At the ends of each array, capture handles are added that provide a mating surface for perpendicular gold hinges that run between arrays, shown in Figure 17. The capture handles have large features that aid manual assembly for this proof of concept design, but these handles could equally be spaces for the integration of an RF receiver, a safety fuse, or other means of switching power on or off to the connected actuators. The large hole in this implementation serves dually as either a rudimentary press fit for a probe tip (see Figure 18), or as a well for an adhesive.

Out of plane hinges

Anchored device
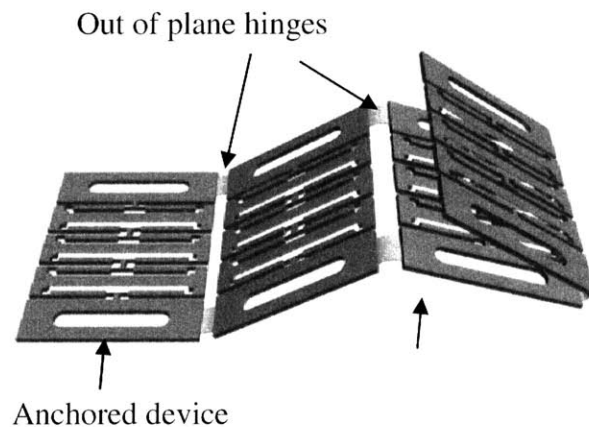
Figure 17: Folding concept for assembly of several strings of actuators.

Gold, when deposited in a thin film, has sufficient ductility and strength to support highly plastic, and therefore low spring-back, out of plane bending, and can be implemented as a flexible hinge for construction of three dimensional shapes from planar components [50]. After the actuator release, the gold hinges form a structural backbone running perpendicular to the direction of actuation. As the substrate is etched away, the gold hinges suspend the arrays over the substrate, satisfying FR_{31}. The length of the gold ribbon is arbitrary, so large numbers of components may be assembled on a single feature without scaling design complexity, satisfying FR_{32}. After release from the substrate, actuator strings are folded about the gold hinges out of plane to assemble many actuator strings in parallel. Once the device is assembled as needed, the hinges can be de-

tethered from the substrate and the device can be delivered to its destination, as shown in Figure 18, and satisfying FR$_{33}$.
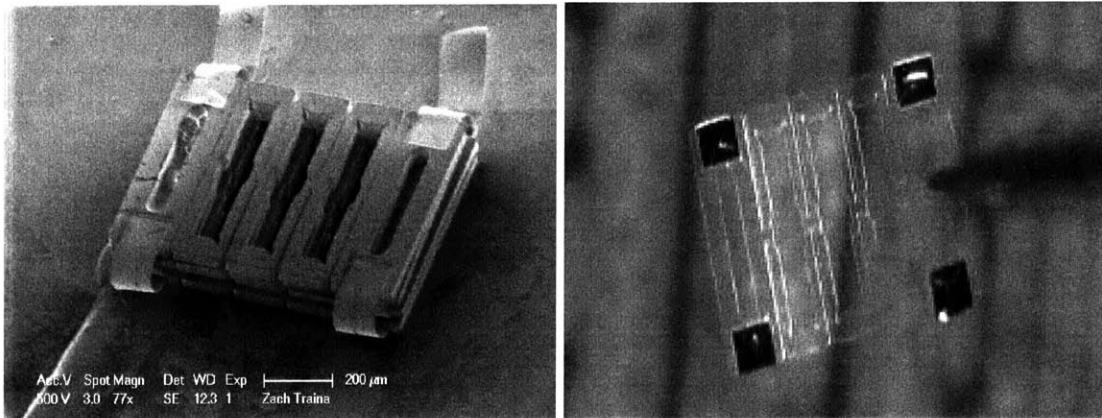
Figure 18: *Left:* Several SU8 test structures rolled about gold hinges and relocated elsewhere on the substrate. *Right:* A single test structure being manipulated via probe tip.

Though it is not required, it is sensible to integrate the wiring of devices with the assembly feature. This physical coupling is simple, though possibly less robust[4], if the gold hinges serve doubly as electrical interconnects. In this implementation a voltage potential is applied to the bottom two hinges in the device. A flexible electrode bus distributes power and signal to each device in the array from the charged gold hinges. Because the power bus is connected on both sides to adjacent actuators in the array, there is no way for them to curl out of plane where they are vulnerable to fracture during assembly out of plane. The wires have short length to prevent residual stresses from causing unwanted deformation. Because the wires running vertically between devices are folded out of plane, they have negligible stiffness.

Each actuator has a redundant source of voltage potential, so the mechanical failure of one connecting wire does not necessarily lead to device failure. Shorting of one device will lead to the shorting of all connected devices, which means that some means of

---

[4] A more robust solution calls for the physical decoupling of the electrical and mechanical connections between devices, discussed in Future Work: Suggested Redesign.

disconnecting the shorted array from the rest of the collection will be necessary for a truly multi-scale device to be realized.

Modular Assembly. Because the long range assembly method and the short range assembly method are completely uncoupled, anything that can be fabricated via 2d lithography and is process compatible with the actuator array can be assembled into the collection. For this proof of concept, only actuator arrays are implemented, but any of the arrays could be replaced with other features, such as extension stops, guiding linkages, protective covers, or features to aid larger scale assembly. Modular assembly at this scale allows many other functionalities to be built into the system without compromising the design of an individual actuator, so long as the materials and processes are compatible with the actuators' manufacturing. Figure 19 and Figure 20 show schematics for a device comprised entirely of actuators and one for which a separate design feature has been substituted.
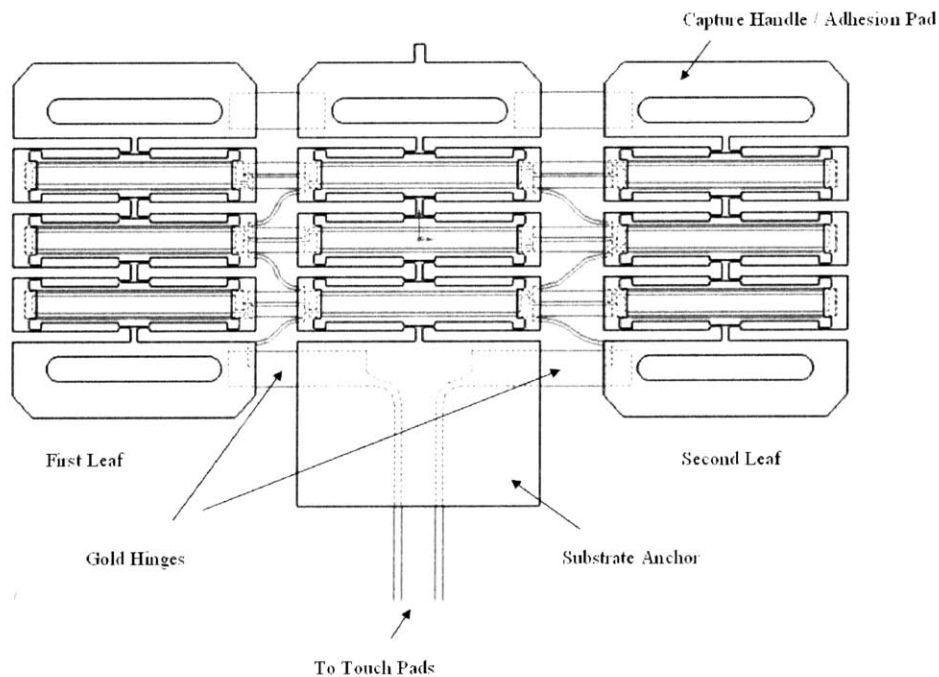
Figure 19: Schematic for a matrix of 9 actuators to be folded out of plane via gold hinges. Wiring and hinges are shown in blue, SU8 shown in black.
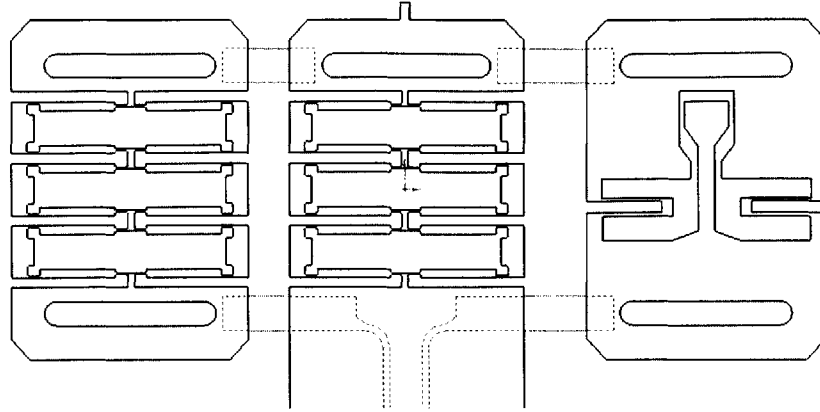
Figure 20: An extension stop fabricated in parallel with two actuator arrays.

Chapter 4

Fabrication

The fabrication process for the folded actuator is shown in Figure 21: Fabrication process for a folded actuator. Additional process detail is given in Appendix A: Fabrication Details.
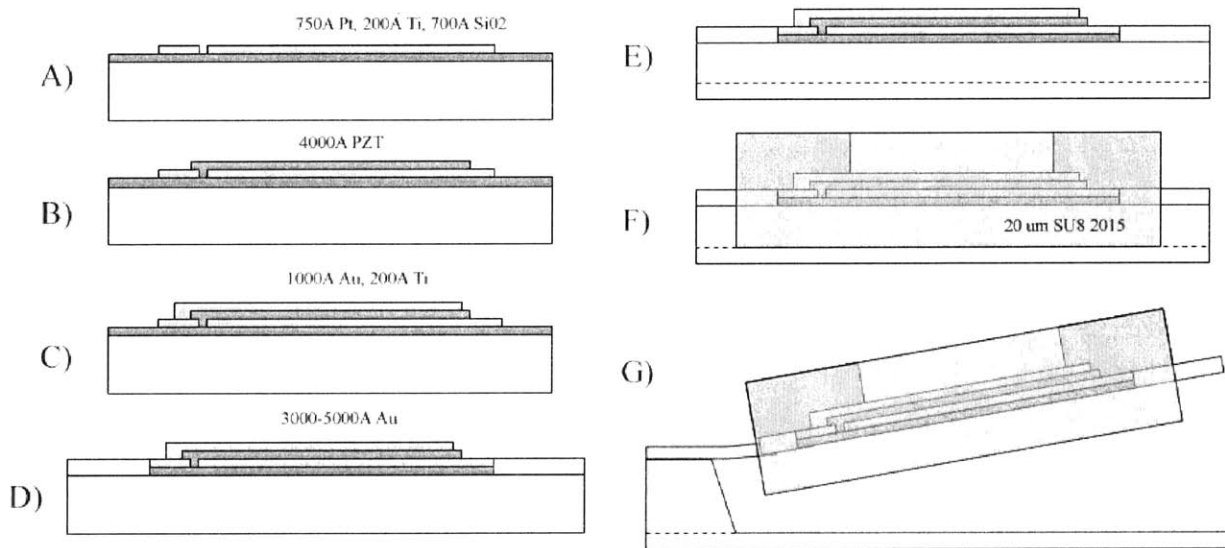
Figure 21: Fabrication process for a folded actuator.

Starting with P-type <100> 4" test grade silicon substrates, SiO_2 is grown to a thickness of 700A via wet thermal oxidation after RCA cleaning.
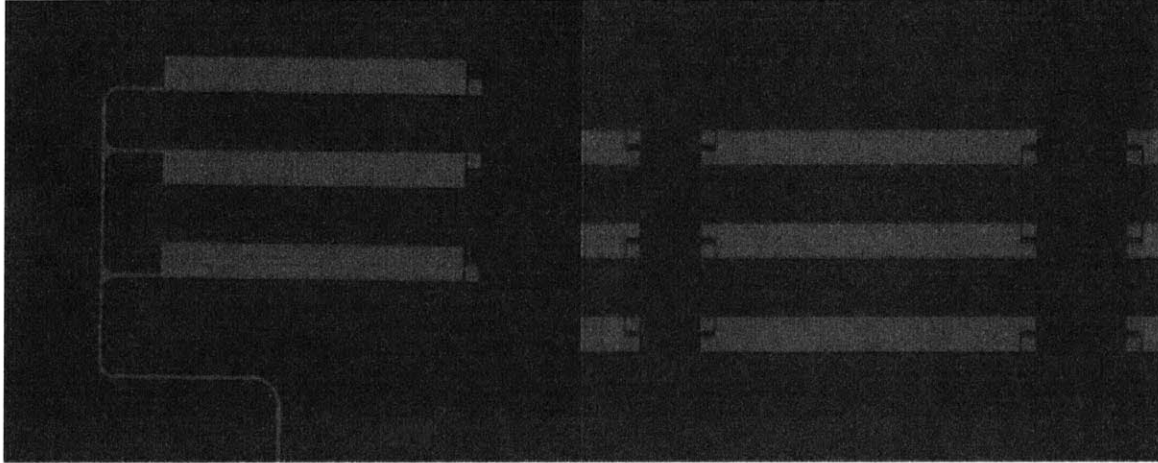
Figure 22: Bottom electrodes of a single (left) and folded (right) device. White areas are platinum, beige background is SiO₂.

In step A), a bottom electrode of Titanium (200A) and Platinum (750A) is then deposited by electron beam evaporation and patterned by liftoff in acetone. Films are deposited at very low vacuum (less than 10^{-7} Torr) and at low speed, 1 A/s, to give satisfactory film uniformity and residual stress. Liftoff in acetone is done overnight, with wafers placed face down in the bath to prevent re-adhesion of cleared features. Light ultrasound agitation is used to dislodge smaller 2 μm features that do not lift off naturally (note, however, that ultrasound has low selectivity to adhesion to resist vs. SiO₂, so strong ultrasound will dislodge the 2 μm features as well as others that were not intended). NMP strong positive resist stripper or plasma ashing may also be used to remove stubborn resist.
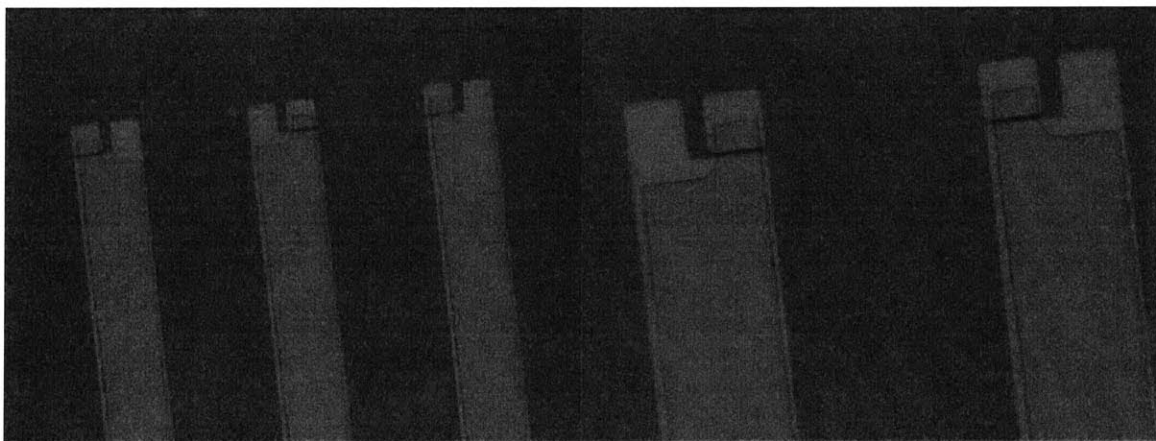
Figure 23: Unannealed PZT after patterning in HF and stripping the passivating resist.

To reduce the occurrence of pinhole shorts, the bottom electrode must be cleaned thoroughly to remove void-forming particle inclusions before the first layer of PZT is deposited. This cleaning consists of 90 seconds of ultrasound washing in acetone, methanol, and DI water, followed by one hour of dehydration at 200C. Following thorough cleaning of the bottom electrode, a Pt seed layer ($PbTiO_3$) is deposited by sol gel at 3000 rpm in step B). The PZT thin film then is spun on from sol gel in 4 layers of .10 um for a total thickness of approximately .4 μm, pyrolyzing at 380C for 5 minutes after the deposition of each layer. The wafer must be covered and immediately dried during and after deposition to limit the number of particle inclusions in the film.

Before annealing, the thin film is patterned via wet etch in 800 DI Water:100 HCl:15 BOE (See Figure 23). The etch rate of PZT in BOE is near instantaneous, even when mixed in these proportions. For this fast etch, OCG 925 Positive thin resist is used in place of the less predictable AZ 5240 P thick resist. The reaction produces a white, non water soluble lead-based particulate, likely a lead halide PbClF [51] that adheres to the wafer and may build up at the edge of the passivating resist. In order to prevent this buildup from causing uneven undercut, the etch is accomplished in several brief bursts separated by vigorous agitation in pure DI water to dislodge the particulate. It has been shown by the same that a chemical reaction may also preferentially remove the particulate, but this process requires several chemicals including Nitric Acid (HNO_3) which, in addition to being hazardous, may have undesirable effects on processes up- or downstream. The multistage etch leads to very good edge linearity to within 1 μm, and also allows better control over the degree of undercut, since the wafer can be visually inspected to measure undercut between etch bursts, and etching can be continued or halted as necessary. After stripping the passivating resist in acetone, the entire substrate is then annealed at 650 C for 20 minutes in a box furnace to complete the PZT process. Hillocking or cracking in the PZT film (if present) is immediately evident by optical inspection.
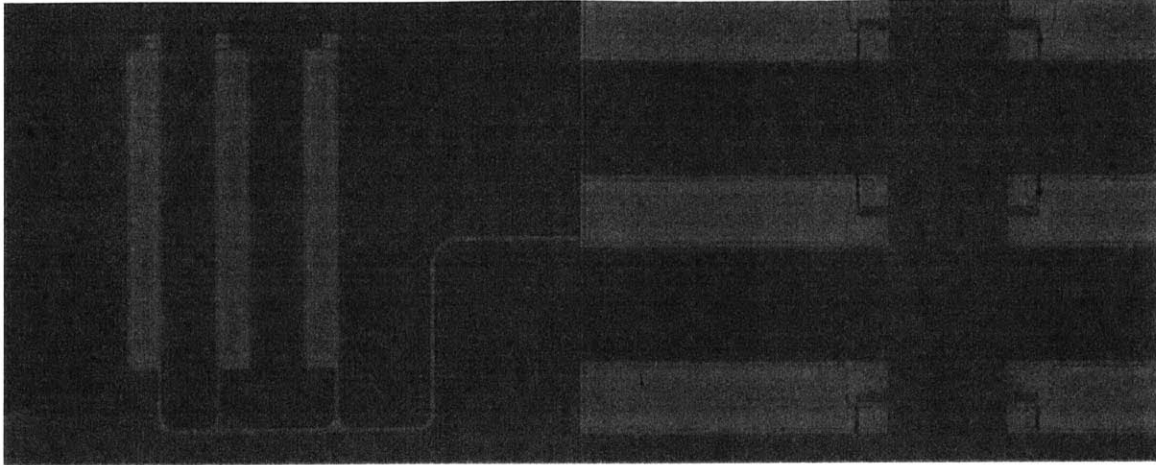
Figure 24: Thin Film PZT growth on the bottom electrode, after annealing.
Note color fringes indicate thickness non-uniformity.

In step C), the top electrode, 200A Ti, 1600A Au, and 200A Ti, is deposited similarly by electron beam evaporation and liftoff. Titanium adhesion layers are used both on the top and bottom of the film to promote adhesion to the PZT layer and the following SU8 layer.
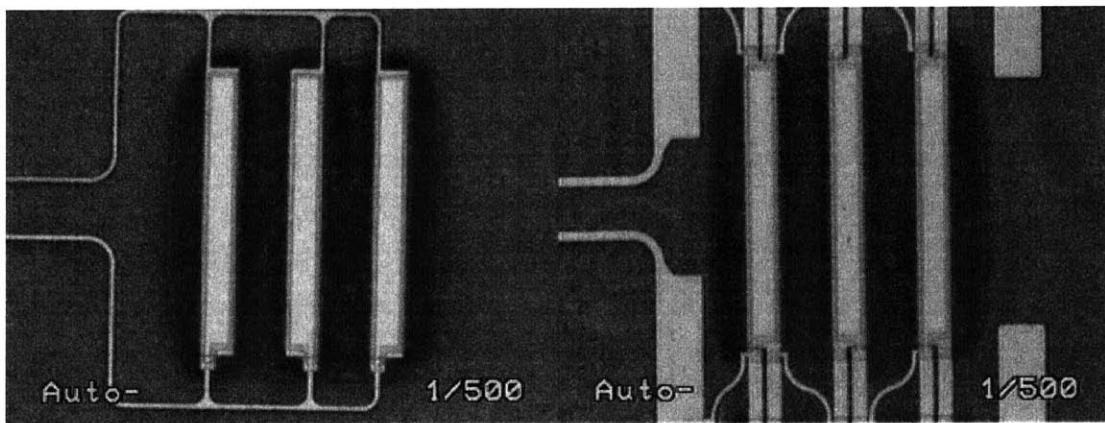
Figure 25: Gold top electrode deposition and RIE etch of the SiO$_2$, leaving brown oxidized Si background. An additional gold deposition layer forms the hinges for the folded device (right).

With the PZT member completed, in step E) the wafer is first dry etched in 10 CF$_4$:0$_2$ in order to remove the thin oxide layer, and then etched in SF$_6$ to create the pockets that will support the SU-8 beam structure.

The beam structure is fabricated in SU-8 Series 2015 in step F), which is spun onto the highly varied substrate surface. Due to the aspect ratio of the features and close proximity of adjoining devices, it may be difficult to completely planarize the wafer with more viscous formulations of SU-8 resist. To better planarize the wafer and prevent voids, multiple thin coats of low viscosity SU-8 may be applied to achieve the total desired thickness. Degassing SU-8 prior to patterning is not a viable option, since the high relative viscosity and low density of SU-8 prevent the film from closing voids formed by escaping air bubbles. Degassing an SU-8 film, therefore, simply enlarges existing voids as air bubbles force the film open during escape. Particular care must be taken during SU-8 processing to ensure that warping and shrinkage are minimized, since compressive stress in the SU-8 will cause a change in the initial state of the actuator, affecting the net amplification ratio. If the residual stress in the film is tensile, the compression of the device on release will buckle the slender PZT beam, and applied voltage will change the curvature of the beam out of plane but will not apply any load to the amplifying structure. Controlling residual stress in the film is a matter of matching exposure and bake times to the film thickness.
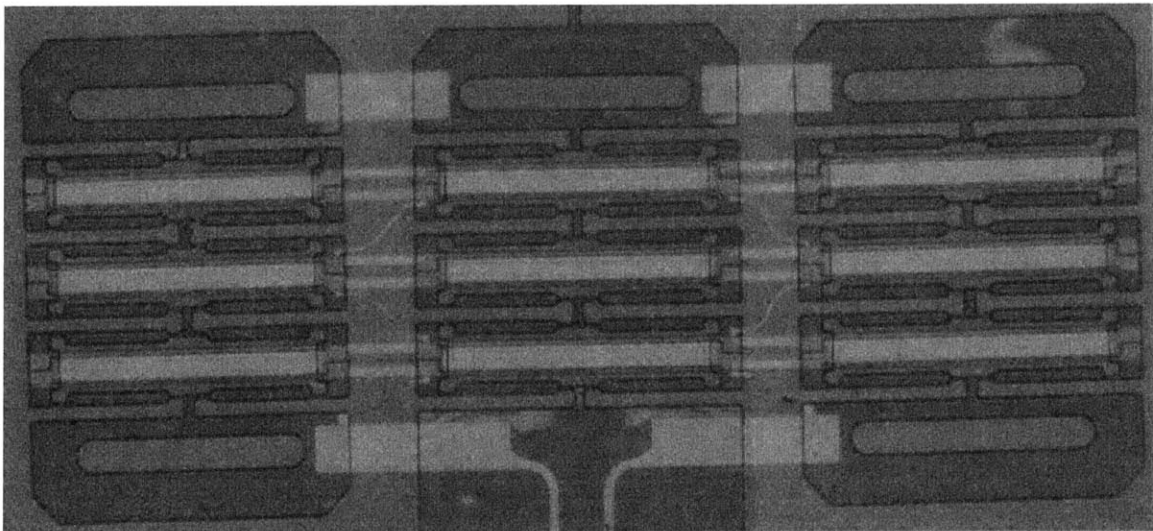
Figure 26: A folded device prior to XeF2 release.
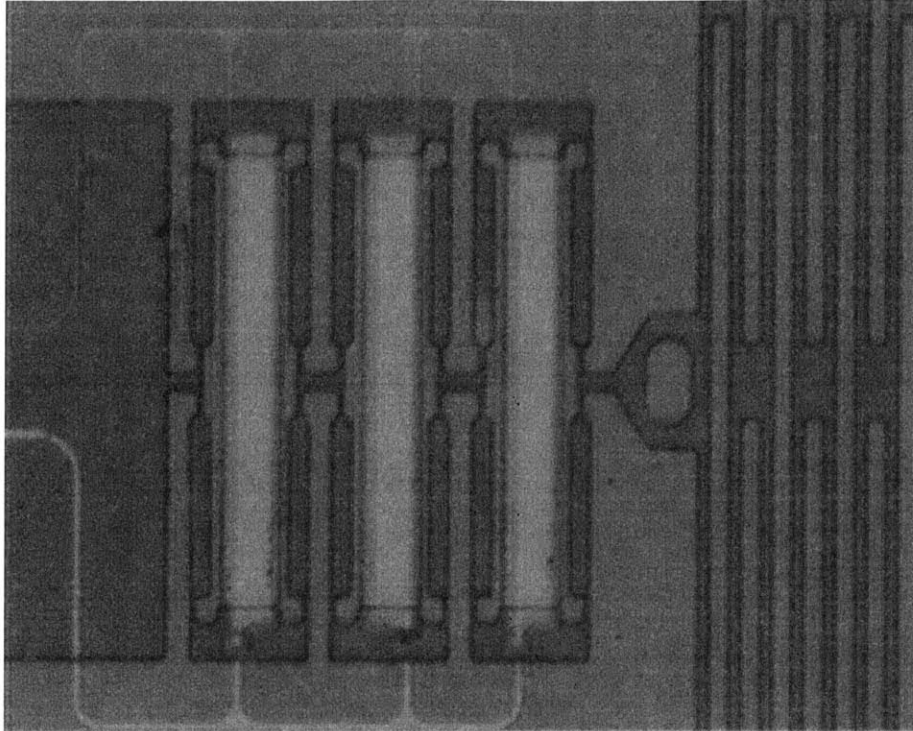
Figure 27: A single actuator triplet prior to XeF_2 release. The structure at right is a double bent spring load used to calculate blocking force.

As the final fabrication step, in step G) the wafer is etched in XeF_2 to entirely suspend the actuator. This dry release step eliminates any possible stiction problems. An SEM of a several contractive cells fabricated in series is shown in Figure 28.
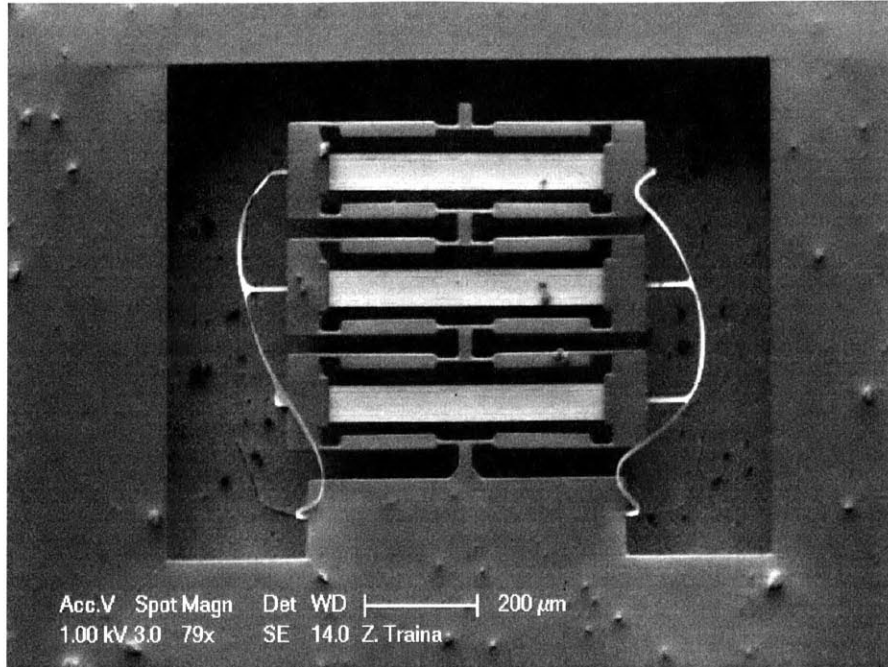
Figure 28: A complete actuator triplet.

For assembly of several triplets, an additional metal deposition is added after the top electrode in step D), before the substrate is dry etched. This metal layer, 200 A Ti or Chromium (Cr), 3000-5000A Au, and 200A Ti or Cr, forms the gold hinges that run between devices. Thicker depositions offer more mechanical strength and additional plasticity during folding, but are less deterministic during manufacturing as thicker films tend to be problematic in lift-off. The Cr or Ti top layer offers additional adhesion to the SU-8 deposition.

Following the release by XeF_2, residual stresses in the gold hinge cause out of plane bending with a moment imbalance strong enough to suspend single actuator triplets above the substrate. From there they may manually folded via probe tip and fastened with adhesive if plasticity is insufficient to combat spring-back in the hinge.

For the assembly of chains of triplets, the residual stress management particularly important since the electrodes are prone to failure as they are strained by the load of the shrinking SU-8. The electrode thickness may be increased to combat this problem, though in the final revision this deposition is coupled to the thickness of the PZT beam, and a thickness increase therefore constitutes additional parasitic losses. Further revisions may decouple this relationship with an additional mask.

Chapter 5

Assembly

Three distinct methods of assembly are investigated for chains of devices like the one in Figure 28. They are

1) Folding. Actuators are folded directly onto one another.

2) Rolling. Actuators are rolled about a large comparative radius.

3) Stacking. Actuators are individually de-tethered and assembled onto locating pins manufactured on a separate substrate.

Folding. Of the assembly methods investigated, folding is by far the most manually intensive per actuator, since devices must be assembled individually and in a specific order. This implies that for large actuator collections, folding is more costly than rolling or stacking techniques, though through folding much smaller collections may be constructed. Folding enables the construction of device collections as small as 6 members, which may be useful for specific applications requiring small form factors.
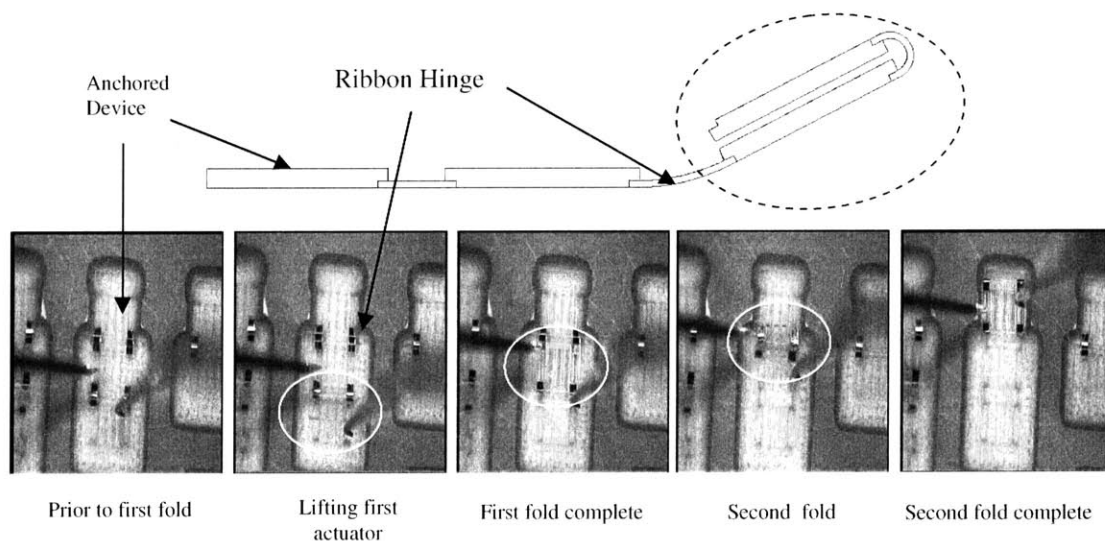
Figure 29: Folding process for several actuator triplets

After the devices are released from the substrate, the last actuator in the chain is manipulated out of plane by the probe tip and then fastened via adhesive at both ends to its neighbor. The pair is then folded onto the next adjacent actuator, adhered, and so on, until the entire collection is folded onto the substrate or de-tethered. The gold hinges constrain the motion of the actuator triplet such that it only has one significant degree of freedom, which is its angle of rotation out of plane. The hinges have varying length to accommodate the larger bend radius of each successive device. This places another practical limit on the number of devices that can be assembled in this way, since large chains of folded devices would require prohibitively large bend radii.

Because of its suitability in constructing small collections, folding was chosen as the assembly method for a demonstration vehicle consisting of 9 actuators. The fully assembled device is shown in Figure 30, where three actuator triplets have been assembled out of plane by manual folding over gold hinges. The device shown was not actuated due to time constraints and the inability to manufacture reliable PZT thin films in parallel over a large area.
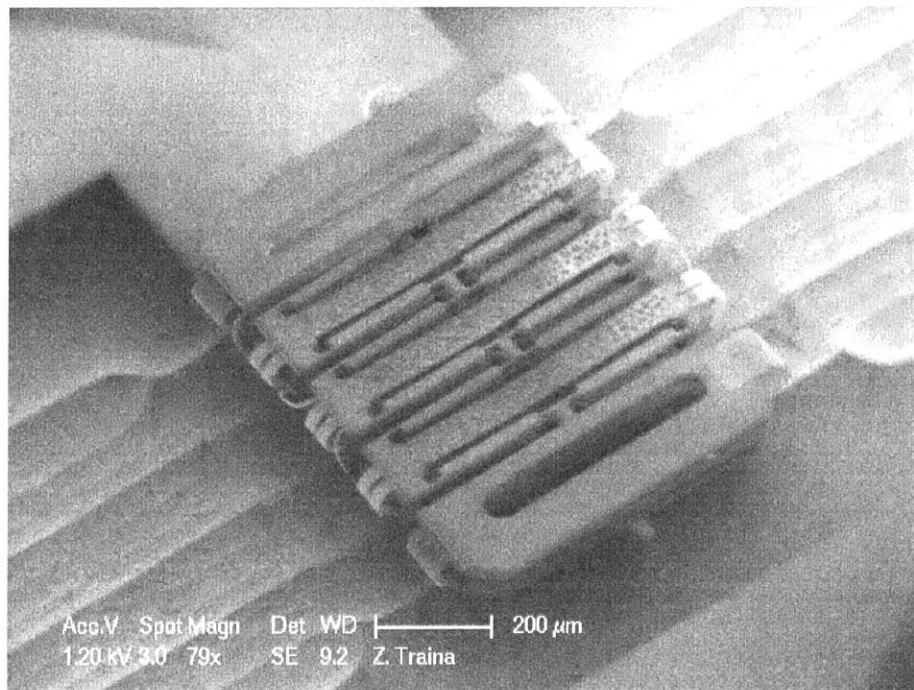
Figure 30: A total of 9 actuators (three actuator triplets) assembled into one collection by folding out of plane over gold hinges. Actuation of a folded device collection is contingent on the manufacturing of functional thin film PZT.

Straight electrical connections run horizontally to power adjacent devices, and thinner semi-helical connections run vertically to power devices in different rows. The hinges are used as electrical interconnects to transfer power from the touch pads (not shown) on the substrate to the first row of suspended devices.

In practice, folding devices about smaller bend radii increases the incidence of delamination between the electrodes (but not the hinges) and the SU8, as apparently the springback force in the hinge overwhelms the adhesion at the interface. This problem may be corrected in future designs by increasing the area of contact between the SU8 and the ends of the electrodes. Removing the SiO_2 from the bottom of the hinge prior to folding did not appear to improve the yield of devices during assembly.

Rolling. Long chains of 20 devices were fabricated on gold ribbons and rolled in a large radius out of the plane of the wafer, shown in Figure 31.
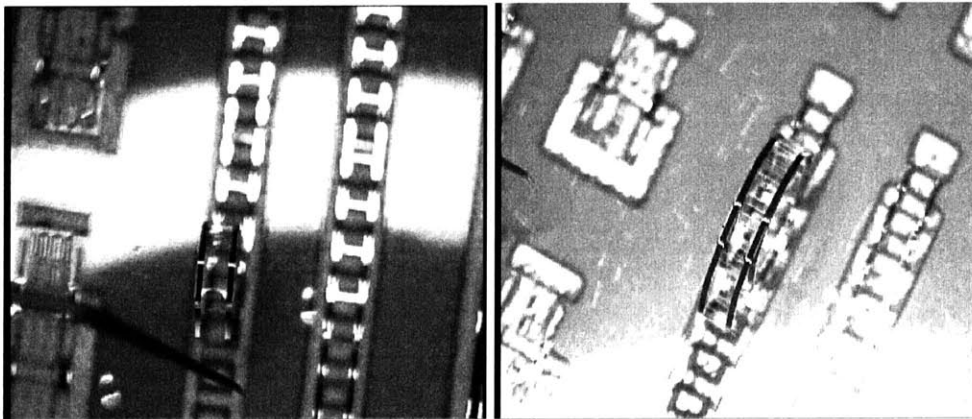
Figure 31: Rolls of long actuator chains. After instigation either by probe tip or gravity, a single revolution forms out of plane (left) and proceeds until the anchored device is reached (right).

To minimize the complexity both in computation and in manufacturing, the devices employed here are simple SU8 boxes with equivalent thickness and outside dimensions of a triplet of actuators. After folding of a few devices at the end of the chain, rolling was instigated either with the probe tip or by tipping the wafer, causing gravity to roll up the remaining devices around the first few. The large inside radii depicted in Figure 31 are due to the fact that the weight of the devices is small compared to the spring force in the hinges. Tighter radii, and therefore more efficient packing, may be possible by affixing a weight, such as a needle, that could act as a heavy mandrill, or by manufacturing thinner

gold hinges. The degree of plasticity in the hinges was small at such a large radius, so the chains could be unrolled and re-rolled elastically.

The assembly time for entire chains of these devices is on the order of seconds, far faster than for folding. Manipulation of the gold ribbon itself or the most distal device in the chain allows a single end effecter to manipulate every other device in the chain simultaneously. This eliminates the manual labor associated with assembling individual actuators, since an entire wafer of devices can be assembled into a collection in a single step, in keeping with FR_{32}. As a corollary to single step assembly, the placement of individual actuators and therefore their alignment to one another is more difficult to control. The packing is also less efficient, since there is a necessary void in the center of the roll.

The chains assembled were ~25 mm long, which validates the durability of the hinge for long range assembly. The strength of the hinges was sufficient to support the weight of the entire chain with the wafer inverted, and survived many 10s of cycles of rolling and unrolling, suggesting that plastic fatigue was not prohibitive at such a large radius.

Stacking. For assembly by stacking, a separate assembly structure was manufactured and devices were imported from their fabrication wafer and stacked on top of one another. Because components can come from entirely different substrates, assembly by stacking allows integration of widely heterogeneous materials and manufacturing processes.

| Maneuvering a freed device | Aligning and stacking 2 triplets | Maneuvering additional triplets | Four stacked sets of actuators |
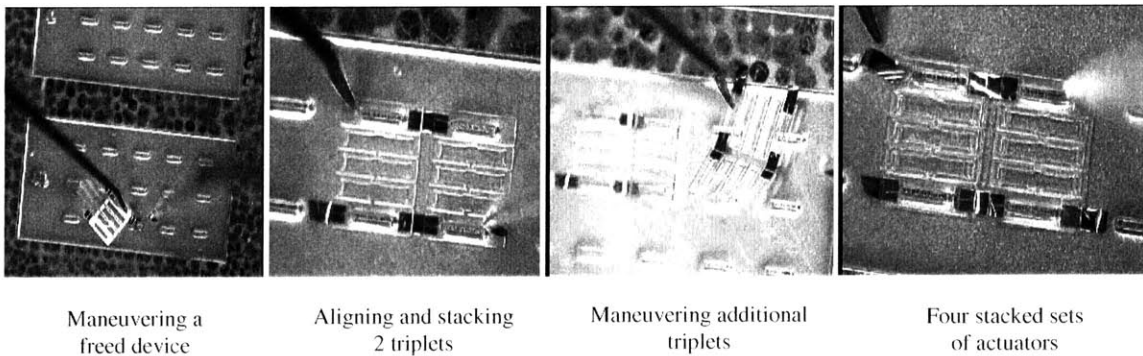
Figure 32: Stacking several actuator sets.

The assembly structure shown in Figure 32 is an array of 150 um tall posts manufactured by DRIE in Silicon. Actuator sets were de-tethered from their original substrate and assembled onto the pins and fastened with adhesive, up to four sets of actuators tall and two wide, for a total of 24 individual units. Again, for fabrication simplicity PZT was not integrated into these units.

With the exception of the application of the adhesive, stacking is a batch assembly process like rolling since entire sheets of actuators can be assembled at once. The pins serve as fine alignment features, while the coarse alignment of the entire sheet is done manually. The limit on the number of devices that can be stacked in this way is only the height of the pin, which is easily designable.

Folding assembly and stacking assembly are commutable, since a chain of actuators can be first folded and then assembled onto the pin array or vice versa. Electrical interconnectivity can be delivered through the pin if it is covered with a conductive coating. However, the manufacturing complexity and the additional uncertainty involved with guaranteeing an electrical connection between every pin and every actuator suggests that the in-plane interconnectivity should be the primary source of power and signal delivery. To minimize assembly effort, entire sheets of actuators should be coarsely aligned onto the assembly jig (pins), allowing the jig to accomplish the fine alignment. The electrical interconnects between sheets can be made between dedicated features specific to each sheet, not each individual actuator.

Chapter 6
Testing and Analysis

A triplet of three devices in series was tested and analyzed to determine its ferroelectric properties and mechanical performance.

X-Ray diffraction (XRD) analysis of the PZT film was performed with a Rigaku 18 KW Rotating Anode 185mm diffractometer to confirm the absence of the pyrochlore phase of PZT. Results of the XRD analysis, shown in Figure 33, confirm the presence of the perovskite (piezoelectric) phase of PZT. Testing was done with an unpatterned wafer segment (structure $PZT/Pt/Ti/SiO_2/Si$) to maximize the signal strength of the PZT film in relation to the underlying platinum and titanium layers, which have very strong phase peaks visible at 40 degrees. The inset image shows that the detrimental pyrochlore phase, if present, is undetectable at 29 degrees.
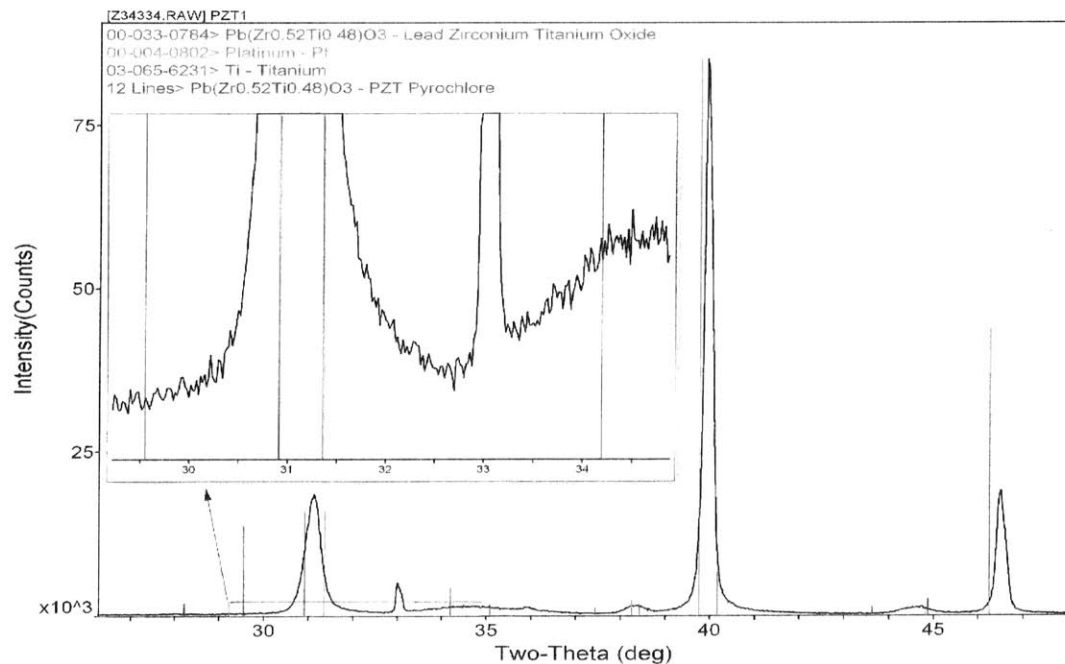
Figure 33: XRD Analysis of a .4um PZT film on Pt/Ti/SiO2/Si.

Because the relationship between deposition thickness and spin speed was unknown at the time of fabrication, profilometry measurements were taken to determine the total film thickness after drying, pyrolysis and annealing. Profilometery data gathered using a P10 Tencor Surface Contact Profilometer are shown in Figure 34. Subtracting the 1000A of underlying Pt/Ti substrate, the thickness of the PZT film is roughly 3000A, with a total variance of no more than 300A. The films appear to have sharp sidewalls and consistent height across all three beams in the device.
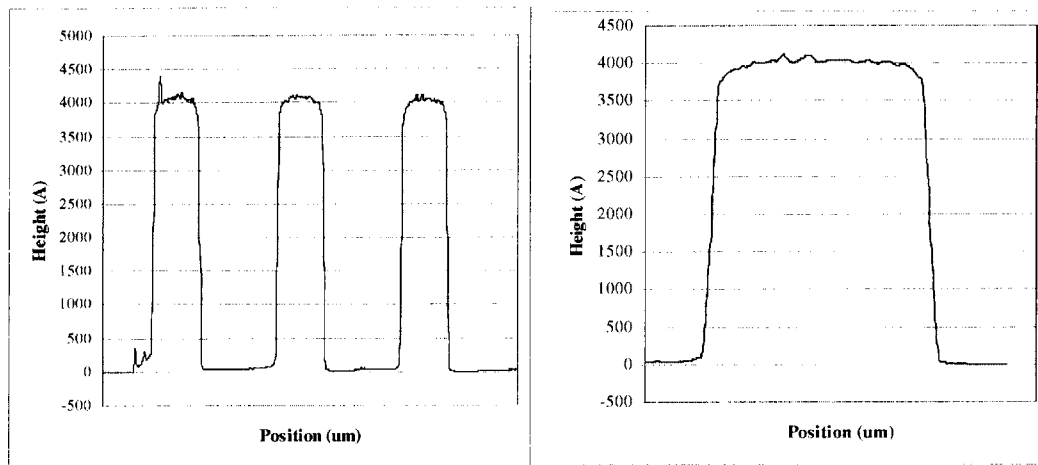
Figure 34: Profilometry of a patterned, annealed PZT film on 1000A Pt/Ti.

The polarization of the PZT film was determined using an RT66A probe station from Radiant Technologies, Inc, of Albequerque, New Mexico, with a PC running Charge 2.3. Devices were poled to voltage limits depending on the total film thickness, consistent with a breakdown voltage of approximately 40V/μm. Results of a 0.4 μm film poled at 15 V are shown below. The remnant polarization of 21.03 μC/cm^2, coercive voltage 3.10V, and saturation polarization of 43.96 μC/cm^2 are all within acceptable limits. The resistance for the final tested device was 1.95 x 10^9 Ohm, with a total leakage current 6.61 x 10^{-9} A for device with non-encapsulated electrodes. This is improved significantly from 1.26 x 10^{-4} A leakage current at 15V developed in the encapsulated device, which has much longer gap length and apparently more avenues for leakage between electrodes.
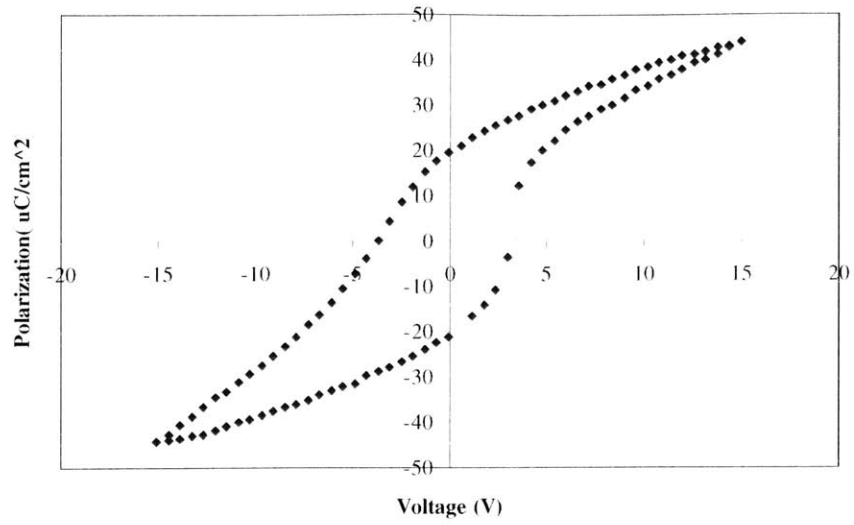
Figure 35: Polarization - Voltage curve for a sample PZT thin film capacitor.
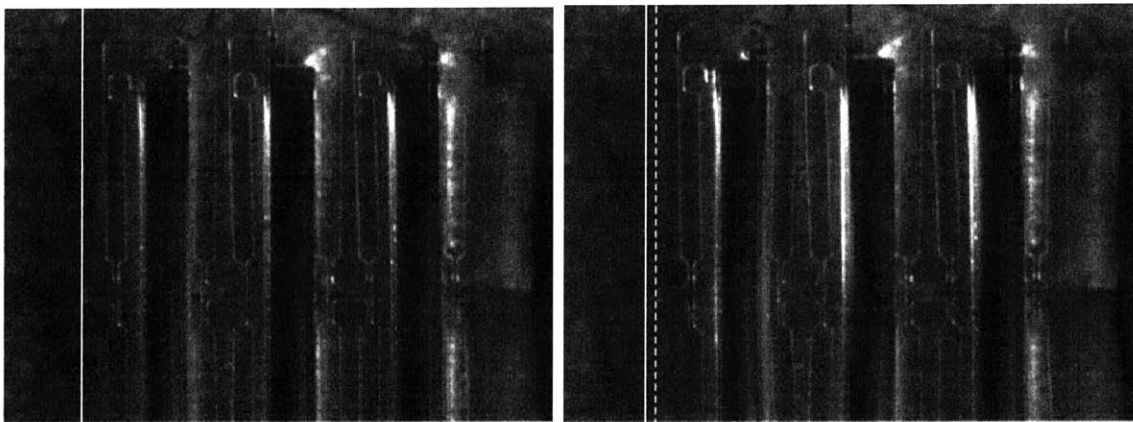
Figure 36: Uncontracted (left) and contracted images (right) of a 3 cell actuator.

$$y = 0.1191x^2 + 0.283x + 0.1277$$
$$R^2 = 0.9936$$

Displacement (um) — Voltage (V)
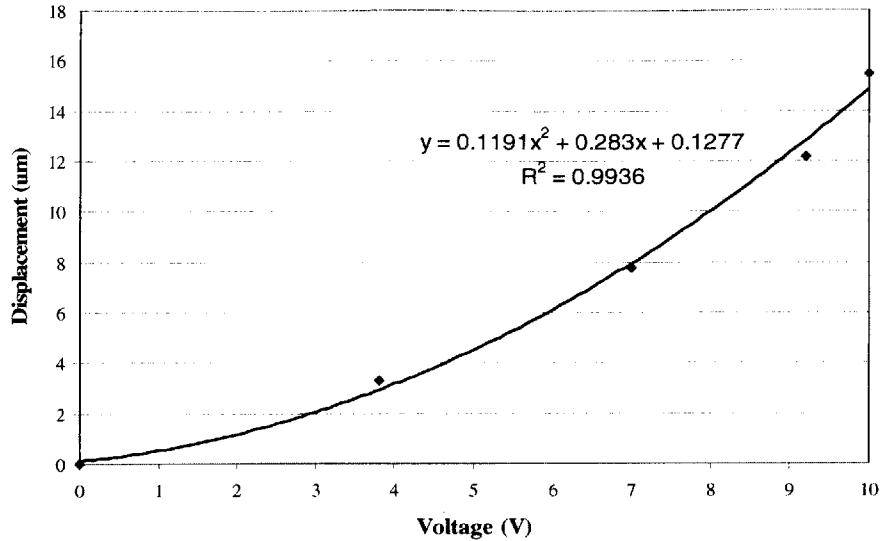
Figure 37: Voltage - Displacement characterization for three contractive actuators in series.

Three actuators fabricated in series were stimulated with a 20V peak to peak, zero offset 0.5 Hz signal and analyzed using an optical Camscope apparatus, with associated software that plots pixel intensities as a function of position. Images of the contracted and un-contracted device are shown in Figure 36, giving the displacement – voltage relationship shown in Figure 37. The 15.24 um displacement corresponds to a 3.01% strain over the 515 length of the un-contracted actuator, which agrees well with the closed form and finite element predictions of maximum unblocked strain for an initial angle of 2.5 degrees, despite the fact that residual stress in the SU-8 likely increases the initial angle.

The blocking force of the triplet is calculated by operating a separate triplet against a double bent spring load fabricated in SU8. The blocking force of the actuator is then extrapolated from force displacement measurements of each. This calculation gives a blocking force equal to 9.21 µN, approximately half the value predicted by closed form analysis. Note however, that this calculation is subject to error due to the possible performance differences between the two devices tested. Though effort was made to test devices of similar electrical characteristics, the mechanical properties of the SU8 (ie elastic modulus) and residual stresses in the other structural layers were not controlled and may give rise to differences in the maximum force or displacement of the two compared devices.

Conclusions

A contractive strain piezoelectric micro-actuator has been designed and fabricated that exhibits an axial strain in excess of 3% under a 10V stimulus. Since the motion of the end effecter is linear and in plane, the device is arrayable in series. Locating the piezoelectric member through the structural center of stiffness removes the eccentric load responsible for out of plane bending. The device may be fabricated either with an open or encapsulated (waterproof) PZT member, though the fabrication of functional PZT may be more difficult in the latter.

The total displacement of the actuator is governed by the amplification of the beam structure and the total input displacement of the PZT member. These two parameters are directly controllable by the initial angle of the beam structure and the stiffness of the laminated electrode. The strain and displacement may be further increased by increasing the device aspect ratio and thickness, but at the cost of reduced energy density.

By use of a flexible gold ribbon, strings of actuators are constrained following their release form the substrate, and can be assembled by rolling, folding, or stacking out of plane about the gold ribbon. Direct fabrication of devices on top of the gold ribbon enables batch assembly, since many devices may be manipulated with a single ribbon. The single greatest impediment in the demonstration of a functional multiscale modular actuator is the ability to fabricate reliable and functional thin film PZT over a wide area.

Chapter 8

Future Work

8.1 Suggestions for Performance Improvement

A thorough investigation of the factors that control consistent PZT thin film growth is needed. In order to reliably and consistently manufacture large areas of PZT in parallel, the factors that instigate PZT failure due to hillocking, cracking, and incorrect or ineffective crystal formation must be determined and controlled. Without deterministic manufacturing of a PZT film, large collections of devices must either be assembled from small modular components that are individually manufactured and tested or be designed to tolerate an imperfect yield of functional devices. Modular assembly of individual components may be prohibitively difficult since the manual labor involved in device manipulation scales directly with the total number of devices. Assemblies that are able to tolerate PZT device failure must have integrated logic or passive intelligence, and additionally will suffer decreased performance proportional to the yield of functional devices in the collection.

Possible factors leading to inconsistency in PZT processing include:

1) Inconsistency in the uniformity and residual stress of the Pt/Ti substrate.
2) Inconsistency in the cleanliness of the substrate prior to sol deposition.
3) Inconsistency in the directionality of the PZT sol due to drying or flow path effects during deposition.
4) Inconsistency in the temperature profile of PZT processing.
5) Variance in the PZT sol supply properties over time.

Observed modes of failure in the PZT film include:

1) Non piezoelectric (dielectric) films
2) Shorted films
3) Leaking films

Films with increased gap length were more likely to have low resistance and therefore increased leakage current when tested. It is assumed that leakage paths form near areas where PZT is grown directly on the SiO₂ substrate, or where particles with low dielectric constants are included in the film during processing. Unusual test results were also recorded when the Pt lower electrode was punctured by the probe tip(s), leading to leakage through the silicon.

4) Hillocking and delamination
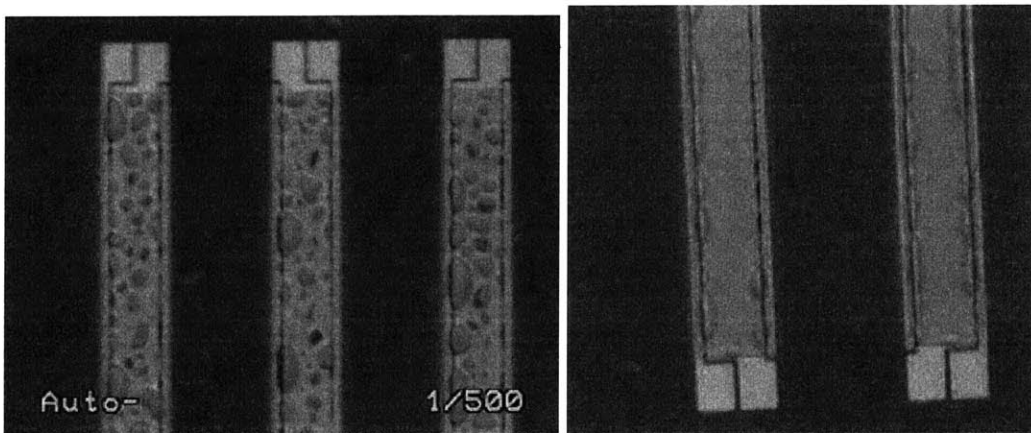
Figure 38: Severe hillocking after the annealing of a .4 um PZT film.

The most common and debilitating PZT film irregularity over the course of this work was delamination and hillocking near the edges of the Pt electrode. Profilometry of a hillocked film shows nearly 100% thickness variation across the entire width.

5) Cracking
6) Degradation or failure of film properties over time

To improve the quality of the film, rapid thermal annealing (RTA) should be employed in place of a box furnace. In addition to being more consistent over time and across each wafer, the temperature profile of a rapid annealer may leave less total time for the stable and non-piezoelectric pyrochlore phase of PZT to form.

8.2 Suggested Redesign

In order to eliminate failure and leakage associated with PZT growth on bare SiO_2, the gap can be entirely removed using a high breakdown voltage, low conductivity jumper, such as by sputtering a thin oxide or by depositing and patterning a thin polymer film such as polyamide. This allows the PZT growth to be confined entirely onto the Pt substrate, and eliminates the need for a very small and intermittently problematic liftoff feature. The increase in the minimum feature size suggests that the new design could be compatible with direct placement patterning techniques like ink jet printing.

PZT deposition over Pt substrate

A)

Non conducting, high breakdown voltage jumper

B)

Pt top electrode deposition over jumper and PZT

C)
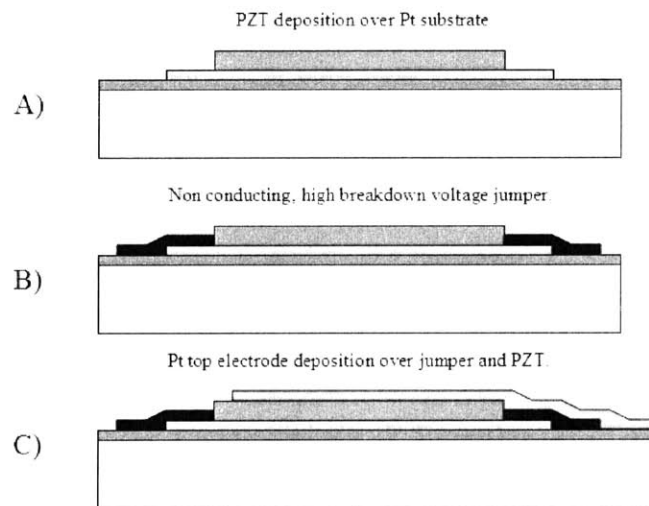
Figure 39: Substitute process plan for a robust PZT member.

For the amplifying mechanism, a new structural material should be selected that meets the functional requirements of the flexure hinge, ie a large ratio of yield strength to elastic modulus. Materials such as silicon, polysilicon or even a thick metal film may perform better as flexure materials while jointly avoiding the residual stress problems in SU8. A more durable flexure would also be less prone to failure during manipulation and assembly. It was previously shown that the stiffness of the amplifying material is not the dominating stiffness in the system, so stiffening this material should have a net positive impact on the device performance.

For simplicity in the current design, wiring is left uncovered and is therefore vulnerable to fracture or de-lamination during assembly. In the near term, a simple solution would be to cover the wiring with a thin, patterned polymer film. As a more

involved, but potentially more robust solution, the connecting wires could be laminated directly on the bottom surface of the amplifying structure, or removed entirely from the in-plane array, and added instead as a separate component during assembly. Stacks of actuators would share power vertically by through vias connected by gold solder beads or conductive adhesive. Consecutive strings of actuators could be physically connected to further reduce exposed wiring and the total number of vias per device. With devices rigidly connected to one another, there would be no need for a center-plane PZT member, since out of plane bending would be constrained by the total thickness of the assembly. At larger scales, devices will have redundant signal and voltage sources, so failure of individual wires will not lead to widespread failure of the device array, since all electrodes will be assembled in parallel and with redundant connections. Gold hinges could still be used as aids in assembly and as the main electrical interconnects.

References

[1] A. Neukermans, R. Ramaswami, "Mems Technology for Optical Networking Applications", IEEE Communications Magazine, January 2001, pp. 62-69.

[2] P Chu, S. Lee and S. Park, "MEMS: the path to Large Optical Crossconnects", IEEE Communications Magazine, March 2002, pp. 80-87.

[3] P.F. van Kessel, L. Hornbeck, R. Meier and M. Douglass, "A MEMS based Projection Display," *Proc. Of the IEEE*, Vol. 86, No. 8, August 1998.

[4] A. Manz, N. Graber, and H. M. Widmer, "Miniaturized total chemical analysis systems: A novel concept for chemical sensing," *Sens. Actuators*, Vol. B1, 1990, pp. 244–248.

[5] A. Manz, D. J. Harrison, E. M. J. Verpoorte, J. C. Fettinger, A. Paulus, H. Ludi, and H. M. Widmer, "Planar chips technology for miniaturization and integration of separation techniques into monitoring systems—Capillary electrophoresis on a chip," *J. Chromatogr.*, Vol. 593, 1992, pp. 253–258.

[6] S. Hirata, Y. Ishii, H. Matoba, and T. Inui, "An Ink- Jet head Using Diaphragm Microactuator", MEMS Proc. 1996, IEEE Ninth Annual International Workshop on Investigation of Micro Structures, Sensors, Actuators, Machines and Systems, 1996.

[7] E. Thielicke and E. Obermeier, "Microactuators and their Technologies", *Mechatronics* Vol. 10, 2000, pp. 431-455.

[8] D. Horsley, R. Horowitz, and A. Pisano, "Microfabricated Electrostatic actuators for hard disk drives," IEEE/ASME Transactions on Mechatronics, Vol. 3, No. 3, 1998, pp. 175-183.

[9] M. Onoda, Y. Kato, H. Shonoka, K Tada, "Artificial Muscle using Conducting Polymers," *Electrical Engineering in Japan*, Vol. 149, No. 4, 2004.

[10] L. Bay, K. West, P. Sommer-Larsen, S. Skaarup, and M. Benslimane, "A Conducting Polymer Artificial Muscle with 12% Linear Strain," *Adv. Mater.*, Vol. 15, No. 3, 2003, pp. 310-313.

[11] P. Krulevitch, A.P. Lee, P.B. Ramsey, J.C. Trevino, J. Hamilton, and M. A. Northrup, "Thin Film Shape Memory Alloy Microactuators," *Journal of Microelectromechanical Systems* Vol. 5, No. 4, 1996, pp 270-282.

[12] R. Pelrine, R. Kornbluh, Q. Pei, and J. Joseph, "High-Speed Electrically Actuated Elastomers with Strain Greater Than 100%," *Science*, Vol. 287, 2000, pp. 836-839.

[13] C. Bolzmacher, J. Biggs, and M. Srinivasan, "Flexible Dielectric Elastomer Actuators for Wearable Human-Machine Interfaces," *Proceedings of SPIE*, Vol. 6168, 2006, pp 1-12.

[14] R. Kornbluh, "Dielectric Elastomer Actuators: Muscles that Morph," *ICASE Lecture Series on Morphing*, NASA Langley Research Center, Hampton VA, August 2001.

[15]   N. J. Conway, Z. Traina and S. G. Kim, "Strain amplifying piezoelectric MEMS actuator." *Journal of Micromechanics and Microengineering,* Vol. 17, 2007, p. 781.

[16]   R.L. Hollis, A.A. Rizzi, "Agile Assembly Architecture: A Platform Technology for Microassembly," Proc. Am. Soc. For Precisions Engineering 19th Annual Meeting, Orlando Fl, October 26-28, 2004.

[17]   K. Tsui, A. Geisberger, M. Ellis, and G. Skidmore "Micromachined End-Effector and techniques for directed MEMS Assembly" *J Micromech Microeng,* Vol. 14, 2004, pp. 542-549.

[18]   N. Dechev, W. Cleghorn, and J. Mills "Microassembly of 3D Microstructures Using a Compliant, Passive Microgripper", *J. MEMS,* Vol. 13, No. 2, 2004, pp. 176-189.

[19]   I. Tahlan, Y. Zhuang, K. Bohringer, K. Pister, and K. Goldberg, "MEMS Fixtures for Handling and Assembly of Microparts", SPIE 1999.

[20]   G. A. Singh, D. Horsely, M. Cohn, A. Pisano, and R. Howe, "Batch transfer of microstructures using flip-chip solder bonding," *J. Microelectromech.Syst.,* Vol. 8, 1999, pp. 27-33.

[21]   K. Pister, M. Judy, S. Burgett and R. Fearing, "Microfabricated Hinges", *Sensors Actuators A,* Vol. 33, 1992, pp. 249-56.

[22]   A. Friedberger and R. S. Muller, "Improved surface-micromachined hinges for fold-out structures," *J. Microelectromech. Syst.,* Vol. 7, 1998, pp. 315-319.

[23]   R. Syms, "A Surface tension powered self-assembly of 3-d micro-optomechanical structures," *J. Microelectromech. Sys.,* Vol. 8, 1999, pp. 448-55.

[24]   P. W. Green, R. R. A. Syms, and E. M. Yeatman, "Demonstration of three-dimensional microstructure self-assembly," *J. Microelectromech. Syst.,* Vol. 4, 1995, pp. 170-176.

[25]   T. Ebefors, J. Ulfstedt-Mattsson, E. Kälvesten, and G. Stemme, "3D micromachined devices based on polyimide joint technology," in *SPIE Symposium on Microelectronics and MEMS,* SPIE Vol. 3892, Gold Coast, Queensland, Australia, October 1999, pp. 118-132.

[26]   Y. W. Yi and C. Liu "Magnetic actuation of hinged microstructures," *J. Microelectromech. Syst.,* Vol. 8, 1999, pp. 10-7.

[27]   Hunter, I.W, and S. Lafontaine. 1992 "A comparison of Muscle with Artificial Actuators," Technical Digest of the IEEE Solid State Sensor and Acuator Workship, Hilton Head, South Caroline, pp 178-185.

[28]   R. N. Castellano and L. G. Feinstein, "Ion-beam deposition of thin films of ferroelectric PZT," *J. Appl. Phys.,* Vol. 50, 1979, pp. 4406-11.

[29]   S. Otsubo *et al,* "Preparation of PZT films by laser ablation", *Japan. J. Appl. Phys.,* Vol. 29, 1990, L133-6.

[30]   D. Roy , S.B. Krupanidhi and J.P. Dougherty, "Excimer laser ablated lead zirconate titanate thin films," *J. Appl.Phys.*, Vol. 69, 1990, pp. 7930–2.

[31]   L. Simon, S. L. Dren and P. Gonnard "PZT and PT screen-printed thick films," *J. Euro Ceramic Society*, Vol. 21, 2001, pp. 1441-1444.

[32]   M. Kojima *et al*, "Chemical vapor deposition of PbTiO3 films," *Japan. J. Appl. Phys.*, Vol. 22, 1990, pp. 14–17.

[33]   B.A. Tuttle *et al*, "Microstructural evolution of PZT thin films prepared by hybrid metallo-organic decomposition," *J. Mater. Res.*, Vol. 7, 1992, pp. 1876–82.

[34]   G. Spierings *et al*, "Preparation and ferroelectric properties of PZT thin films by spin coating and metalorganic decomposition," *J. Appl. Phys.*, Vol. 70, 1992, pp. 2290–8.

[35]   P. Murlat, "Ferroelectric Thin Films for micro sensors and actuators: a review" *J. Micromech. Microeng*, Vol. 10, 2000, pp. 136-146.

[36]   K.G. Brooks, I.M. Reaney, R. Klissurka, Y. Huang, L. Bursill, N. Setter, "Orientation of rapid thermally annealed lead zirconate titanate thin films on (111) Pt substrates", *J. Mater. Res.*, Vol. 9, Issue 10, 1994, p. 2540.

[37]   G.J. Willems *et al*, "Nucleation and orientation of sol-gel PZT thin films on Pt electrodes", *Integrated FerroelectricsI*, Vol. 15, 1997, pp. 19-28.

[38]   D.P. Vijay and S.B. Desu, "Electrodes for PZT ferroelectric thin films", *J. Electrochem Soc.*, Vol. 140, 1993, pp. 2640-4.

[39]   J.S. Wright and L.F. Francis, "Phase Development in Si Modified Sol–Gel- Derived Lead Titanate," *J. Mater. Res.*, Vol 8, Issue 7, 1993, pp. 1712–20.

[40]   R.J. Ong and D.A. Payne, "Chemical Solution Deposition of PZT Thin Layers on Silicon: Densification and Stress Development," *Br. Ceram. Trans.*, Vol. 103, Issue 2, 2004, pp. 97–100.

[41]   R.J. Ong R and D.A. Payne, "Processing Effects for Integrated PZT; Residual Stress, Thickness, and Dielectric Properties" *J. Am. Ceram. Soc.*, Vol. 88, Issue 10, 2005, pp. 2839-2847.

[42]   C. Niezrecki, D. Brei, S. Balakrishnan and A. Moskalik, "Piezoelectric Actuation: State of the Art", *Shock and Vibration Digest*, Vol. 33, No. 4, July 2001, pp. 269-280.

[43]   N. Lebontiu, E Garcia. Mechanics of Microelectromechanical Systems. Kluwer Academic Publishers, New York, New York, 2005, pp. 293-307.

[44]   W. Xu and T King, "Flexure hinges for piezoactuator displacement amplifiers – flexibility, accuracy, and stress considerations," *Precision Engineering* 19:4-10 1996.

[45]   S.T. Smith. Flexure Elements of Elastic Mechanisms. Gordon and Breach Science Publishers, 2000.

[46]   J. F. Shepard Jr., S. Trolier-McKinstry, M. A. Hendrickson, and R. Zeto, "Properties of PZT Thin Films as a Function of In-Plane Biaxial Stress"; ISAF '96. Proceedings of the Tenth IEEE International Symposium on the Applications of Ferroelectrics, Vol. 1, Edited by B. M. Kulwicki, A. Amin, and A. Safari. IEEE, East Brunswick, NJ. 1996, pp. 161–5.

[47]   D.P. Birnie, R.N. Vogt, M.N. Orr, J.R. Schifko, "Coating uniformity and device applicability of spin coated sol-gel PZT films," *Microelectronic Engineering*, Vol. 29, 1995, pp. 189-192.

[48]   B.H. Chen, C.L. Huang and L. Wu, "Crack alleviation processing of lead zirconate titanate thin films deposited by sol-gel method," *Thin Solid Films*, Vol. 441, 2003, pp. 13-18.

[49]   Y. Jeon, C.W. Wong, and S.G. Kim, "Water-Immersible Micromachined $Pb(Zr, Ti)O_3$ Thin Film Actuators," *Journal of Electroceramics*, Vol. 13, 2004 pp. 509-513.

[50]   H.J. In, S, Kumar, Y. Shao-Horn, and G. Barbastathis, "Nanostructured Origami 3D Fabrication and Assembly of Electromechanical Energy Storage Devices", Proceedings of 2005 5th IEEE Conference on Nanotechnology, Nagoya Japan, Jul 2005.

[51]   K. Zheng, J. Lu, and J. Chu, "A Novel Wet Etching Process of $Pb(Zr, Ti)O_3$ Thin Films for Applications in Microelectromechanical Systems," *Japanese Journal of Applied Physics*, Vol. 43, No. 6b, 2004, pp. 3934-3937.

Appendix A: Microactuator Fabrication Details

Beginning substrate:

P-type <100> 4" Silicon 1-side polished, 425-475 um thickness, TTV < 3 um, Bow & Warp < 10 um, 1-50 Ω-cm

Step 1: **Cleaning of the wafer**
- RCA cleaning

Step 2: **Thermal Oxide Layer**

- A2 tube
- Target deposition 1000A SiO2 (typical thickness ends up around 700A)
- Note: PECVD Oxide not used due to incompatibility with PZT structure

Step 3: **Bottom Electrode Deposition and Lift-off**
- Image reversal photo and develop
  - After HMDS, spin coat resist AZ 5214E, recipe: 6sec@0.5krpm, 6sec@0.75krpm, 30sec@4500 rpm
  - Prebake (30min, 90°C)
  - Expose (EV1 with mask; 1.4sec)
  - Post Exposure bake 30 min 90 C
  - Flood exposure without mask: (45sec on EV1)
  - Develop (MIF 422 90 sec)
  - Location: TRL, coater / oven / EV1

- Target deposition: 200A Ti (Deposition rate: 1A/s) and <500°C substrate temperature
- Target deposition: 750A Platinum (Deposition rate: 1A/s)
- Note: Very clean surface needed.
- Location: TRL e-beamFP

- Acetone lift-off on bottom electrode; followed by methanol and 2-propanol for cleaning.
- Ultrasonic ~2-3mins for quicker lift-off and clearing lift-off residues. Check for possible peel-off.
- Cleaning of solvents and contaminants with: acetone / methanol / 2-propanol and **multiple** rinse dumps.

Step 4: **PZT Deposition, etch and anneal**
- Spin-coat Mitsubishi PZT sol-gel: Pb(Zr,Ti)O$_3$
- Location: MTL PZT spin-coater in TRL
- PZT deposition: spin-coat 500rpm for 3s, 3000rpm for 15s, hot plate drying (pyrolysis) at 380C for 5mins after 1 min 80 C dry
- Notes: for 0.48um PZT layer, use 4 separate coatings, each ~0.12um

- Positive photo and develop
  - After HMDS, spin coat resist OCG 925, recipe: : 6sec@0.5krpm, 6sec@0.75krpm, 30sec@3000 rpm

- Prebake (30min, 90°C)
- Expose (EV1 with mask; 2.3 sec)
- Develop (OCG 1:1 925 until clear)
- Post Exposure bake 30 min 120 C
- Location: TRL, coater / oven / EV1
- Wet etch unnanealed PZT 100 HCL:15 BOE: 800 DI water, 4 sets of 3 seconds with agitation in DI water between etches to dislodge particulate.
- Location: acid hood
- Strip resist in acetone, propanol, methanol

- PZT furnace 1st Annealing : at 650C for 20min
- Location: TRL PZT furnace

Step 5: **Top Electrode Deposition and Lift-off**
- Image reversal photo and develop
  - After HMDS, spin coat resist AZ 5214E, recipe: 6sec@0.5krpm, 6sec@0.75krpm, 30sec@1500 rpm
  - Prebake (30min, 90°C)
  - Expose (EV1 with mask; 1.4sec)
  - Post Exposure bake 30 min 90 C
  - Flood exposure without mask: (50sec on EV1)
  - Develop (MIF 422 90 sec)
  - Location: TRL, coater / oven / EV1

- Target deposition: 200A Ti (Deposition rate: 1A/s)
- Target deposition: 1000A Au (Deposition rate: 3A/s)
- Note: Very clean surface needed.
- Location: TRL e-beam

- Acetone lift-off on bottom electrode; followed by methanol and 2-propanol for cleaning.

Step 6: **Hinge Deposition and Lift-off**
- Image reversal photo and develop
  - After HMDS, spin coat resist AZ 5214E, recipe: 6sec@0.5krpm, 6sec@0.75krpm, 30sec@1500 rpm
  - Prebake (30min, 90°C)
  - Expose (EV1 with mask; 1.4sec)
  - Post Exposure bake 30 min 90 C
  - Flood exposure without mask: (50sec on EV1)
  - Develop (MIF 422 90 sec)
  - Location: TRL, coater / oven / EV1

- Target deposition: 200A Ti (Deposition rate: 1A/s) and <500°C substrate temperature
- Target deposition: 5000A Au (Deposition rate: 3A/s)
- Note: Very clean surface needed.
- Location: TRL e-beam

- Acetone lift-off on bottom electrode; followed by methanol and 2-propanol for cleaning.

Step 7: **Create lower beam structure**
- RIE with 10 O_2: CF_4 for 400 sec to clear oxide, Location: Plasmaquest
- DRIE with SF_6 to create deep pockets, 8 min recipe Ole3. Location: STS1 Au.

Step 8: **Create Su8 beam structure**

- Dehydrate bake: 200C for at least 10 min
- Spin on 20 um of Su8: SU8 spinner in TRL photo, 500 Rpm 20 sec spread, 30 sec 2250 rpm spin
- Softbake: hotplate 3:30 min @ 95°C
- Expose with EV1 in TRL photo, 5 sets 4.5 sec with 15 sec rest
- Post-exposure bake: hotplate 4:30 min @ 95°C
- Develop with PM Acetate in Photo-Wet Au ~4-6 min

Step 9: **XeF2 release etch**

- Release structure using XeF2 etch, approx 120 cycles of 60 sec etch time, depending on etch rate.
- (XeF2 is an easy process, but the etch rate changes everytime. After 1st 100sec etch is complete, eye inspection followed by proper main etch is recommended)

Appendix B: Detailed Mask Designs
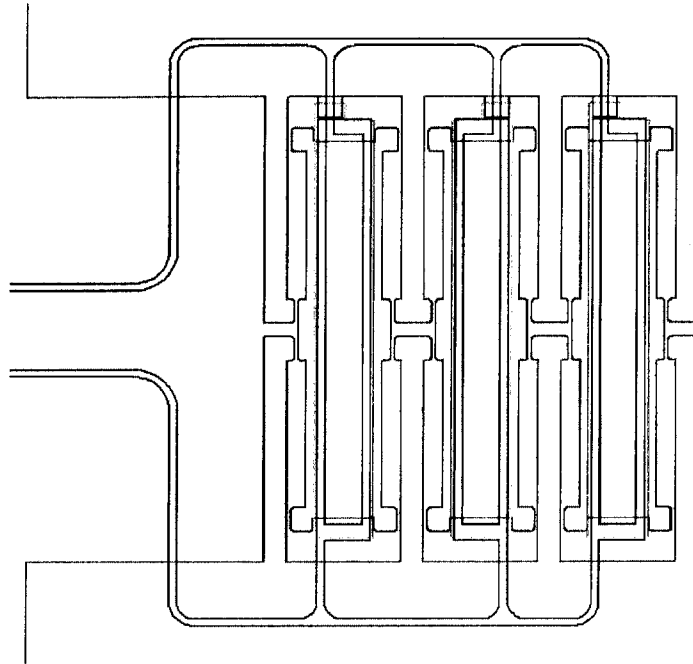
Figure 40: Single triplet. no load. Top electrode is show in blue, SU8 in red, PZT in light green, and the bottom electrode in darker green.
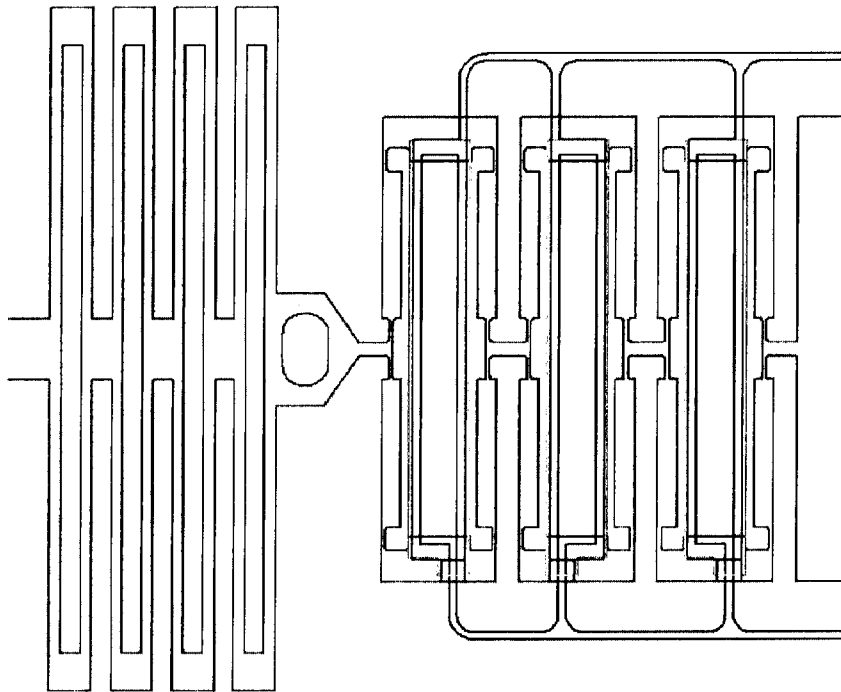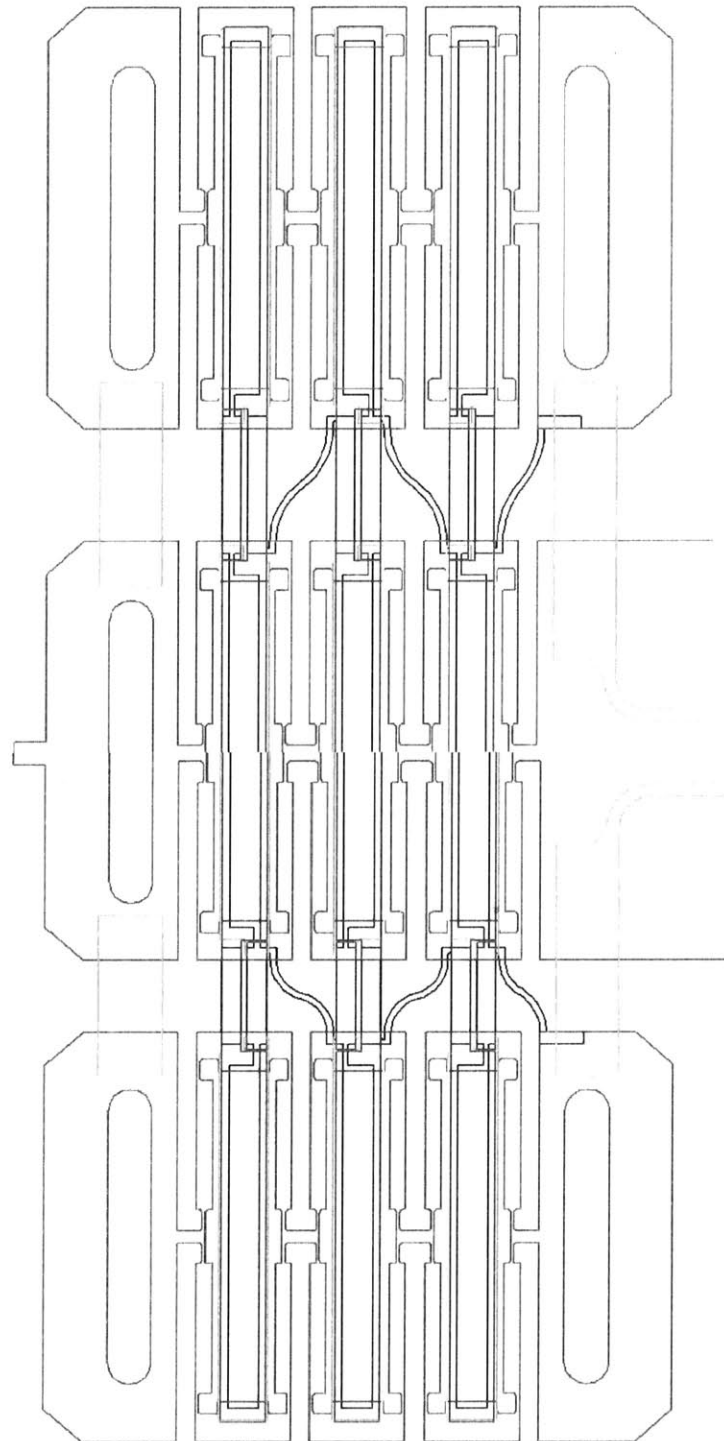

Figure 41: Single triplet, loaded.

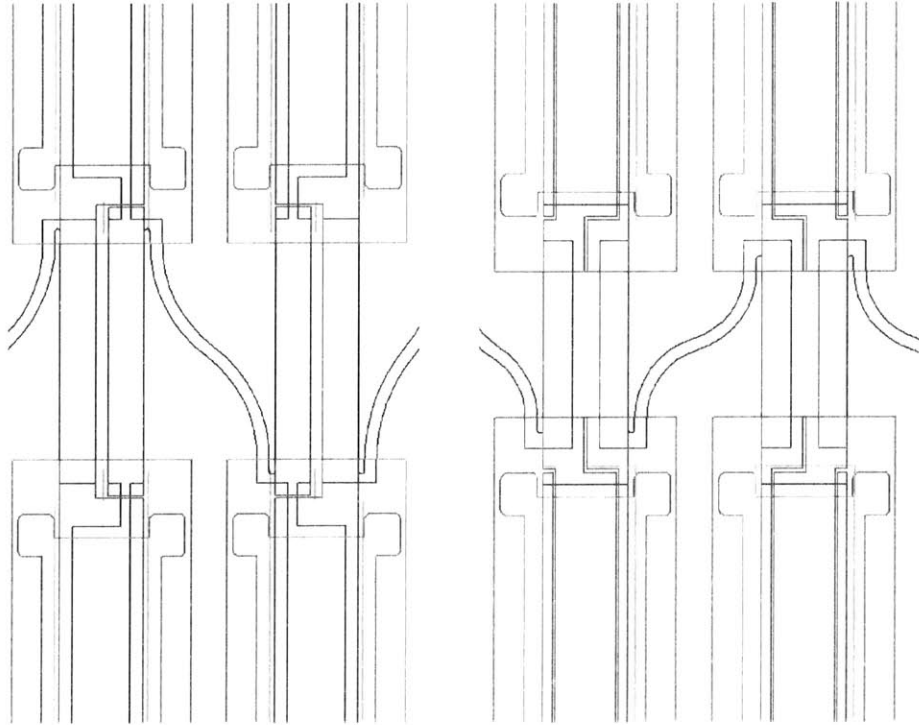**Figure 42:** Folded device, no load. Open PZT beam design. Hinges drawn in orange.

Figure 43: Open (left) and encapsualted (right) PZT beam designs. Spacing between SU8 differs since the bend radii are not the same (images were taken from different parts of each device.)
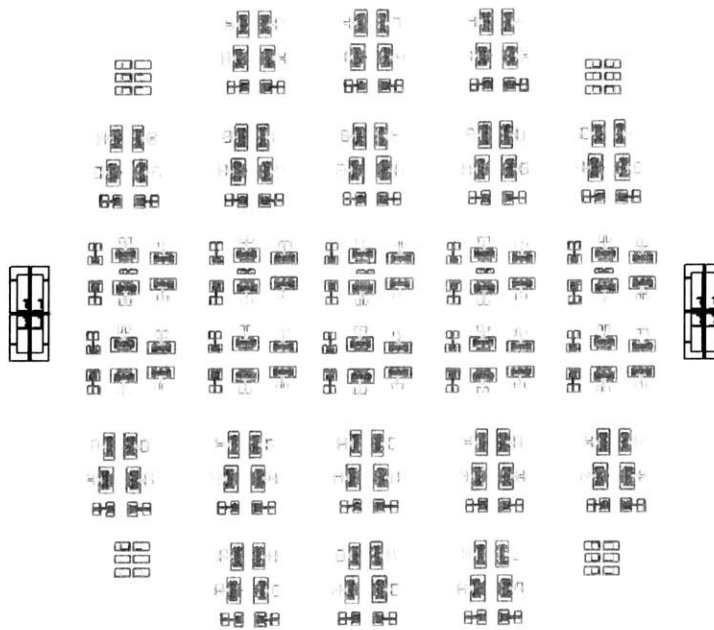

Figure 44: Diceable 4" mask layout.

Appendix C: Executive Summary

A Large Strain, Arrayable Piezoelectric Microcellular Actuator by Folding Assembly

Z.J. Traina, S.G. Kim

A low power, piezoelectric, contracting cellular MEMS actuator has been developed that demonstrates a peak strain of 3% under a 10 V stimulus. Since the motion of the end effecter is linear and in-plane, the actuator can be arrayed in series to amplify the total stroke or in parallel to amplify the total force as needed. Location of the piezoelectric member through the structural center of stiffness reduces the potential for parasitic out of plane bending present in previous designs [1].

Cellular actuators arrays can be assembled into a larger array of actuators. We demonstrated sets of cellular microactuators can be assembled out of plane by folding them over thin gold hinges. To our knowledge, this is the first effort in this field. The gold hinges serve dually as mechanical assembly guides and electrical interconnects. Long chains of devices may be assembled by rolling out of plane. A smaller collection is shown in Figure 2, assembled by folding three actuator triplets onto one another. Actuation of the collection is contingent on the manufacturing of functional thin film PZT.
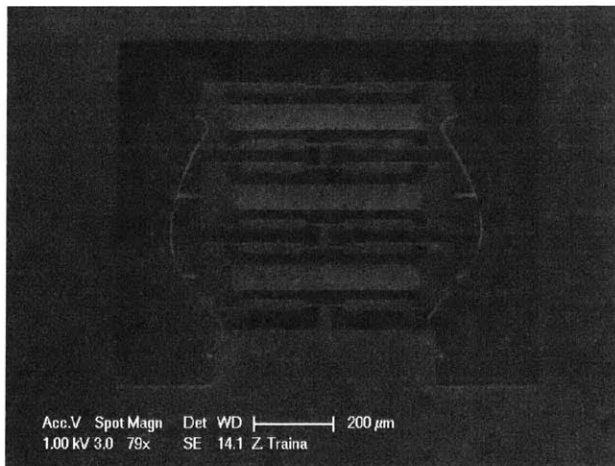

Figure 1: An array of three cellular actuators fabricated in series, which demonstrates a total static displacement of more than 15 μm under 10V stimulus. The strain of the assembly exceeds that of unmodified PZT by a factor of more than 29:1.
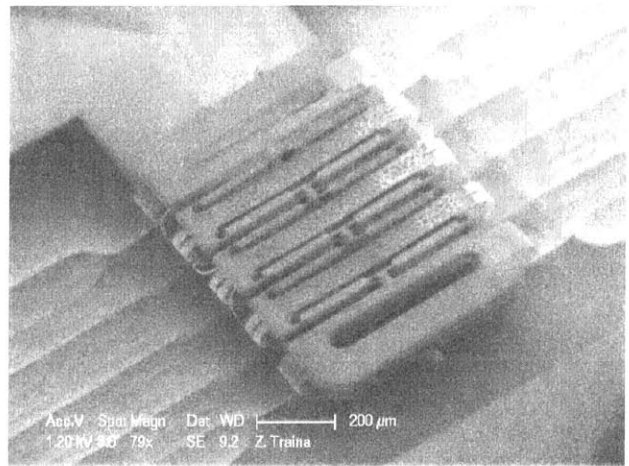

Figure 2: A total of 9 actuators (three actuator triplets) assembled into one collection by folding out of plane over gold hinges. Actuation of a folded device collection is contingent on the manufacturing of functional thin film PZT.

REFERENCES

[52] N. J. Conway, Z. Traina and S. G. Kim, "Strain amplifying piezoelectric MEMS actuator," *Journal of Micromechanics and Microengineering*, Vol. 17, P. 781, 2007